CDF/ANAL/CDF/CDFR/2049[1]

Measurement of Small Angle Antiproton-Proton Elastic Scattering at $\sqrt{s}$=546 and 1800 GeV

S. Belforte, G. Chiarelli, P. Giromini,
S. Miscetti and R. Paoletti

April 22, 1993

Abstract

Antiproton-proton elastic scattering was measured at c.m.s. energies $\sqrt{s}$ = 546 and 1800 GeV in the range of four-momentum transfer 0.025< $-t$ <0.25 GeV^2. The data are well described by the exponential form e^{bt} with slope b=15.2±0.6 (17.0±0.25) GeV^{-2} at $\sqrt{s}$=546 (1800) GeV. The elastic scattering cross sections are, respectively, σ_{el} =12.9±0.3 and 20.0±0.9 mb.

During the 1988-1989 physics run of the Fermilab Tevatron Collider, the $\bar{p}p$ elastic scattering differential cross section was measured in the four-momentum transfer range 0.025< $-t$ <0.25 GeV^2 at c.m.s. energies $\sqrt{s}$=546 and 1800 GeV. The data were taken in short dedicated runs, in which the Tevatron lattice was adjusted to provide low-t detection over a wide t-range at each energy. After an initial run at $\sqrt{s}$=1800, one run at $\sqrt{s}$=546 was followed immediately by a second run at $\sqrt{s}$=1800. At these energies, the average scattering angle is a fraction of a $m$rad. Therefore, this measurement required to bring detectors as close as 4 mm to the beam-axis with an accuracy of $\simeq$ 10μm and at distances of $\simeq$30 m from the interaction region; as the detectors lay

[1]to be submitted to Phys. Rev. D

in between several Tevatron magnets, a precision measurement required the determination of the transport matrices of this sector of the machine to one part in a thousand.

I. EXPERIMENTAL METHOD

A top view of the experimental layout is shown in Fig. 1. Elastically scattered particles were observed by a magnetic spectrometer composed of two arms in the (horizontal) x-plane of the machine: arm-1 detected elastic events in which the $\bar{p}(p)$ was scattered towards the inside (outside) of the beam-orbit; with respect to the beam z-axis, symmetrically scattered elastic events were detected by arm-0. We call *west* the outgoing $\bar{p}$ side (positive z-axis) and *east* the outgoing p side; y is the vertical axis pointing up. In each arm, the $\bar{p}$-trajectory was measured at three different z-positions along the beam line by detectors S1, S2 and S3 , while the p-path was determined by the S6 and S7 detectors. In elastic events, the proton and antiproton are collinear and one detector on each side would be enough to make a measurement. Redundancy was chosen to guarantee full efficiency and to reduce systematical errors. All detectors were placed inside special sections of the beam pipe with variable aperture. Once stable beam conditions were reached, the detectors were displaced horizontally towards the circulating beam. The beam was scraped until the detectors could reach the desired positions. Detector displacements were monitored with an accuracy better than 10 μm. From survey measurements, the detector distances from the machine magnetic-axis were known to ± 0.1 mm; distances from the interaction point were determined to ± 1 cm and distances between two detectors in different arms at the same z-location

were surveyed to within 70 μm.

Elastically scattered recoils travelled across the quadrupole magnets q_0, q_1 and q_2. The magnets q_1 defocussed in the horizontal plane , while q_2 acted as a focussing lens. The string of the four quadrupoles q_0 on each side of the interaction region provided high luminosity by squeezing the betatron function at the interaction region to a value $\beta \simeq 0.5$ m (low-β). In the $\sqrt{s}$=546 run, the magnets q_0 were almost at full power. In the two $\sqrt{s}$=1800 runs, the q_0's were powered off and β was about 80 m at the interaction region (high-β). Using the standard formalism of transfer matrices, the elastic recoil coordinates at a given z_i-position are

$$x_i = \varepsilon_i^h \cdot x_0 + L_i^h \cdot \theta_x \qquad (1)$$

$$y_i = \varepsilon_i^v \cdot y_0 + L_i^v \cdot \theta_y$$

where (x_0, y_0) are the coordinates at z=0 and θ is the scattering angle. Values of the transfer matrix elements (ε_i,L_i) at the z-position of each detector are listed in Table 1. Each spectrometer detector (Fig. 2) comprised a drift chamber and a silicon detector sandwiched by two trigger counters and had an active area $\Delta x \cdot \Delta y = 3.5 \cdot 3.0$ cm^2. The drift chambers [1] had four wires measuring the x-coordinate of a track at four different z-positions. The sense wires induced a delay line, that measured the y-coordinate by the time difference at the two ends. The drift measurement provided single-hit accuracy of 110 μm and double-hit resolution of 3 mm, while the single-hit accuracy of the delay line was 480 μm and the double-hit resolution about 2 cm.

The 0.9 mm thick silicon detector [2] had double sided segmented read-out. The anode (ohmic side) consisted of 64 Al strips 50 μm wide, spaced by 500 μm. By not completely depleting the diode, the x-position was measured by the charge division method. The

cathode (barrier side) measured the y-position with 30 gold pads 900 μm wide, spaced by 100 μm. The x-resolution of the silicon detector turned out to be slightly worse than the pitch itself, but the double-hit resolution (1.0 mm in x and y) was very useful. The correlation between the charge collected by the cathode strips and by the anode pads allowed unambiguous reconstruction of multi-hit events. The accuracy (a few microns) to which the electrode positions were known allowed a good calibration of the drift velocity and of the delay line propagation time for every chamber. During the data taking we lost some silicon channels; apart from that, both chamber and silicon detectors were 100% efficient (see Appendix A). The redundancy of active devices in each detector guaranteed full efficiency. The trigger for elastic events required the coincidence of all ten counters in each arm. To ensure full efficiency, test data were taken before each run and the voltage of each counter was adjusted so that its full pulse height spectrum was above threshold (see also Appendix A).

II. DATA REDUCTION

A. EVENT RECONSTRUCTION

We first reconstructed (x,y) points in every detector. In the silicon, we looked at the strips and reconstructed all charge clusters. For every cluster the x-position (x_{sil}) was derived by charge weighting; by correlating the charges of the x-clusters and of the y-pads, space points were reconstructed. In the drift chamber, the x-position was derived by requiring at least two out of four wires to have the same drift time (x_{drift}). Unambiguous space points were then derived by looking at the delay line information

and requiring the condition $T=t_{d1}+t_{d2}-2t_d$, where T is the transit time of the full delay line, t_d is the drift time measured by the sense wires and t_{d1}, t_{d2} are the times measured at the ends of the delay line. For every detector, we merged space points in the chamber and in the silicon, averaging by error weighting those points within four sigma. In 90% of the cases, points were found both by the chamber and the silicon. In 8% of the cases, the x-coordinate was not reconstructed in the silicon (dead channels, but the y-coordinate was available), while in 2% of the cases the y-coordinate was not measured by the chambers but only by the silicon.

B. GEOMETRICAL ALIGNMENT OF THE DETECTORS AND DETERMINATION OF THE MACHINE LATTICE FUNCTIONS

In order to define a precise trajectory with the space points measured by the detectors, the spectrometer alignment was improved relative to the survey using the data. Details of the spectrometer alignment procedure are given in Appendix B. Within the available statistics, the x-coordinate scale for each detector was determined to two parts in a thousand (70 μ over 3.5 cm) ; the y-coordinate scale was known to within one part in ten thousand. By using the simulation, we derived a systematical error of $\leq$0.1% on the measurement of the slope b and of the optical point $dN_{el}/dt|_{t=0}$; because these errors are correlated, the resulting systematical error on the total elastic rate $N_{el} = \frac{dN_{el}/dt|_{t=0}}{b}$ was negligible .

At $\sqrt{s}$=546 (1800), the minimum angle detected by the spectrometers was determined to within 0.48 (0.38) μrad, putting a limit of 0.07% (0.17%) on the systematical error of the extrapolation to the optical point.

The machine nominal momentum was known to within 0.12% from the measurement of the integrated field of all Tevatron magnets and from the average radius of the closed orbit given by the RF frequency value [3]; the consequent systematical errors in the determination of the slope and of the optical point are listed in Table 6. The lattice transport matrices were determined as described in Appendix C. Several $\simeq$1% adjustments to the nominal Tevatron optics were made; within our statistics, the transport matrix elements were relatively adjusted to better than one part in a thousand. A systematical error of 0.15% on the absolute value of the lattice functions could not be excluded. By using our simulation, at $\sqrt{s}$=546 (1800) we derived a systematical error of 0.1% (0.1%) for the slope value, 0.4% (0.2%) for the the optical point and 0.3% (0.3%) for the total elastic rate. At $\sqrt{s}$=546, when constraining the slope b to be 15.35$\pm$0.2 GeV^{-2} (see section IV), the systematical errors on the optical point and on the total elastic rate were reduced to 0.2%. All systematical errors are summarized in Table 6.

C. DATA FILTERING

We collected 34552 and 38759 elastic triggers at $\sqrt{s}$=546 and 1800, respectively. We rejected events if any trigger counter was out of time by more then $\pm$ 5 ns (TOF FILTER) in order to eliminate triggers from satellite bunches spaced by $\pm$20 ns with respect to main bunches. Events lost by this cut or because of early accidental hits in the counters were evaluated by pulsing all counters during data taking to simulate elastic event triggers and counting the number of missing or rejected pulser triggers ; the loss was $\simeq$1.0% and is listed in Table 3.

A fraction of our triggers was due to random coincidences of two beam halo particles going in opposite directions through the *east* and *west* sides of one spectrometer arm. These halo particles, which passed on time in one side (*west/east*) of one spectrometer arm, were in most cases also detected at an earlier time by the drift chambers of the other spectrometer arm on the opposite side (*east/west*). The number of tagged and rejected halo events is listed in Table 2 (HALO FILTER).

We then looked at the hit multiplicity in the various detectors and we rejected events in which both S1 or S2 had more than two hits in the triggering arm, if S1+S2 in the other arm had three counters out of four fired and more than four y-hits in anyone of the silicon detectors. The same requirement (HIT FILTER) was applied to S6 and S7. On the *east* side (S6,S7), this filter rejected all elastic events travelling at an angle smaller than that subtended by the detectors and interacting in the vacuum chamber separating the detectors from the beam; it also rejected low mass diffractive events. On the *west* side (S1,S2), the filter rejected triggers caused by beam losses. The number of events rejected by this filter is listed in Table 2; the filter efficiency for retaining good events (100%) is discussed in Appendix A. Corrections for event losses due to nuclear interactions in the detectors ($\simeq$1.8$\pm$0.2%) were also applied, as listed in Table 3 and discussed in Appendix A.

In the remaining events, we used the following procedure to reconstruct the vertex coordinates (x_0,y_0) at z=0 and the antiproton (proton) scattering angle $\theta_{\bar{p}(p)}$. We required at least one point in both *east* and *west* sides of a spectrometer; the points on the *east* side ought to lie inside a 250 μrad cone around the straight line passing through the points on the *west* side and x=y=0 at z=0 (ROAD FILTER) (see Table 2). On the *west* side, when S3 and (S1 and/or S2) were present, we reconstructed the

$\bar{p}$ trajectory by determining (x_0,y_0) and $\theta_{\bar{p}}$ with eq.(1). Then, by using (x_0, y_0) and the points measured by S6 and/or S7, θ_p was also determined with eq.(1). When S3 or S1 and S2 were missing (see Table 4), we assumed x_0=y_0=0. In cases where some detectors had more than one point (usually a δ-ray in only one detector), by assuming x_0=y_0=0, we first determined all possible combinations of points in different detectors that lay within a road. In most cases, this procedure was sufficient to reject spurious hits. For all combinations of points in different roads, we reconstructed the proton and antiproton trajectories as described above. If more than one combination was left (see Table 5), we selected the one with the best collinearity.

D. BACKGROUND EVALUATION AND REMOVAL

Fig. 3 shows the y_0 vs. x_0 distributions for all events at $\sqrt{s}$=546 and 1800 GeV. A 3.5 sigma vertex cut was applied to reduce the background contamination. Fig. 4 compares collinearity ($\Delta\theta = \theta_{\bar{p}} - \theta_p$) distributions for the events accepted and for those rejected by the vertex cut. Events lost by this cut ($\leq$0.2%) were accounted for in the acceptance calculation. Fig. 5 shows $\Delta\theta_y$ vs. $\Delta\theta_x$ collinearity plots for all events passing the vertex cut. The solid lines indicate the collinearity cut defining our final sample of elastic events; events lost by this cut ($\leq$0.2%) were also accounted for in the acceptance calculation. The residual background contamination ($\leq$0.5%, as listed in Table 3) was estimated from the events with $\Delta\theta_x$ outside the dashed lines in Fig. 5; Fig. 6 shows the $\Delta\theta_y$-distribution for these events, normalized at $\Delta\theta_y$ outside the dashed line to the $\Delta\theta_y$-distribution of events inside the $|\Delta\theta_x|$ collinearity cut. The amount of background counted inside the $|\Delta\theta_y|$ collinearity cut was then statistically

removed. Fig. 7 shows dN/dt distributions for all events within the collinearity cut and for the removed background.

E. BEAM TILT-ANGLE DETERMINATION

The angle of the beam with respect to the spectrometer axis (tilt-angle) was determined using the data. In the y-z plane, where the spectrometer covers negative and positive angles around θ_y=0, we adjusted the spectrometers by an angular tilt equal to the mean value of the θ_y-distribution. In the x-z plane the spectrometer did not cover the angular region around θ_x=0. In order to determine the tilt angle, we calculated the spectrometer acceptance for several angles of the beam with respect to the spectrometer-axis (see Appendix D for a description of the simulation). For each tilt-angle, we fitted the t-distribution of the data corrected by the corresponding acceptance, independently for arm-0 and arm-1, with the form $\frac{dN_{el}}{dt}|_{t=0}e^{bt}$. We adjusted the spectrometer by the tilt-angle that minimized the differences between the $\frac{dN_{el}}{dt}|_{t=0}$ and b values determined by the fits in the two spectrometer arms. As shown in Fig. 8, the values of b, $dN_{el}/dt|_{t=0}$ and N_{el} do not depend on the beam tilt-angle when fitting both arms simultaneously. As a check, once we adjusted the tilt-angle, we selected all events with $|\theta_y| \leq 400$ μrad and, after correcting for acceptance, we fit the $dN_{el}/d\theta_x$ distribution with the form $Ke^{-b(\theta_x-\theta_0)^2}$ and verified that the tilt-angle θ_0 from the fit was consistent with zero within 1.0 μrad.

III. DATA FITTING

The t-acceptance of the spectrometer was calculated for a fiducial region defined by eliminating all events within 0.5 mm from the detector boundaries. The t-distribution of the data, corrected for acceptance, was fit with the exponential form $A \cdot e^{bt}$, with $A = L \cdot \frac{d\sigma_{el}}{dt}|_{t=0}$; an exponential t-dependence is expected for a nucleon density with gaussian distribution [4]. This fit functional form was corrected for the Coulomb scattering contribution [5]

$$1 + \frac{4\pi\alpha^2(\hbar c)^2 G^4(t)}{A|t|^2} e^{b|t|} + \frac{\alpha(\rho - \alpha\Phi)\sigma_T G^2(t)}{A|t|} e^{b|t|/2}$$

where the nucleon form factor was parametrized as $G(t) = (1 + |t|/(0.71\ \mathrm{GeV}^2))^{-2}$ and the relative phase as $\Phi(t) = -0.577 + \ln(k|t|^{-1})$, α is the fine structure constant, σ_T the total cross section and k=0.08 (0.07) GeV^2 at $\sqrt{s}$=546 (1800) GeV. Assuming the ratio of the real to imaginary part of the nuclear elastic scattering to be ρ=0.15, the Coulomb scattering contribution was $\simeq$ 1.0% at the lowest t.

At $\sqrt{s}$=1800, the spectrometer t-resolution ($\sigma_t \simeq 0.009\ \mathrm{GeV}\cdot\sqrt{-t}$) was smaller than the Δt=0.01 GeV^2 bin width used in the fit and no smearing was applied when fitting the observed t-distribution. At $\sqrt{s}$=546, where $\sigma_t \simeq 0.019\ \mathrm{GeV}\cdot\sqrt{-t}$ was comparable to the Δt=0.0025 GeV^2 bin width used in the fit, smearing corrections ($\simeq$0.3%) were applied by fitting the functional form $A(1 - b^2(0.019\ GeV)^2/2)e^{bt(1-b(0.019\ GeV)^2/2)}$. Fits at $\sqrt{s}$=546 and 1800 GeV are shown in Fig. 9.

IV. RESULTS AND CONCLUSIONS

At $\sqrt{s}$=546, our value of the elastic slope b=15.2$\pm$0.58 ($\pm$0.09 syst.) GeV^{-2} in the range 0.025$<-t<$0.08 GeV^2 is consistent with the UA4 value b=15.3$\pm$0.3 GeV^{-2} at $|t|<$0.1 GeV^2 [6] and with the recent UA4/2 result b=15.4$\pm$0.2 GeV^{-2} in the range 0.00075$<-t<$0.12 GeV^{-2} [7].

In order to obtain the optical point and the total number of elastic events, we made use of these more accurate measurements of the slope by fitting our data with the additional requirement that the slope be 15.35$\pm$0.2 GeV^{-2}. At the same energy, the total number of elastic events $\frac{dN_{el}/dt|_{t=0}}{b}$ was increased by 0.9% to account for changes of the slope at $t \geq$0.1 GeV^2 as listed in Ref.[6]. At $\sqrt{s}$=1800, similar changes of the slope (b=15.0 GeV^{-2} at $t \geq$0.25 GeV^2) would produce a 0.2% change of the total number of elastic events, which was taken as systematical error on the total number of elastic events at $\sqrt{s}$=1800 due to our limited t-range.

At $\sqrt{s}$=1800, our measurement of the elastic slope b = 17.0$\pm$0.25 GeV^{-2} (0.24 GeV^{-2} statistical and 0.05 GeV^{-2} systematical) in the range 0.04$<-t<$0.25 GeV^2 improves by a factor two the accuracy of the E710 measurement b = 16.99$\pm$0.47 GeV^{-2} in the range 0.001$<-t<$0.143 GeV [8]. By making use of our measurement of the luminosity [9], we determine the total elastic scattering cross section to be σ_{el}=12.9$\pm$0.3 (20.0$\pm$0.9) at $\sqrt{s}$=546 (1800) GeV. Results are listed in Table 7. Our results on the slope parameter at low momentum transfer are presented in Fig. 10 together with other $\bar{p}p$ experiments in the same t range. Assuming an s-dependence of the slope $b = b_0 + 2\alpha' \ln(s/s_0)$, the data at $\sqrt{s}$=546 and 1800 GeV yield α'=0.34$\pm$0.07. A fit including also the ISR data in Fig. 10 yields α'=0.26$\pm$0.02.

ACKNOWLEDGEMENTS

We thank the Fermilab Accelerator Division for the construction and operation of the Tevatron and of the Antiproton Source. In particular, we feel indebted to Craig McClure, who interfaced our spectrometer hardware to the accelerator control system, and to D. Finley and H. Jostlein for many useful suggestions. We wish to thank the Fermilab Computer division, the technical staff of CDF and of the collaborating Institutions for their contribution to the construction and operation of CDF. The dedicated effort of the many technicians and engineers at Frascati and Rockefeller, who contributed to the design, construction and installation of the spectrometer and of the forward tracking vertex detectors, is warmly acknowledged; we especially thank M. Biagioli, G. Bisogni, A. Ceccarelli, M. DiVirgilio, G. Fontana, R. Heidecker, D. Humbert, E. Iacuessa, P. Locchi, A. Rutili, G. Sensolini, D. Scepanovich and M. Troiani. We are grateful to G. Tonelli and E. Focardi who lead the construction of our silicon detectors. This work was supported by the Department of Energy, the National Science Foundation, the Istituto Nazionale di Fisica Nucleare and the Ministry of Science, Culture and Education of Japan.

APPENDIX A. CHECKS OF DETECTOR EFFICIENCY

A. COUNTER EFFICIENCY

The trigger for elastic events required the coincidence of all ten counters in each arm. We checked the trigger efficiency with the data by selecting, in inelastic and diffractive trigger events, single tracks detected by the chamber and the silicon in every detector S1, S2, S3, S6 and S7. We collected about 7500 such tracks in every run. For all tracks, the two counters sandwiching the tracking detectors always had an ADC pulse height consistent with a minimum ionizing particle. For every run, the counter efficiency was found larger than 99.99%. By looking at the TDC information, we determined that the trigger lost about 1.0% of the events, consistent with the pulser corrections (TOF losses) listed in Table 3.

B. EFFICIENCY OF TRACKING DETECTORS AND OF FILTERS

Table 4 shows a negligible uncorrelated probability of losing a good event because of tracking detector inefficiencies. Our analysis resolved all multi-hit events. We studied our analysis filters as the only possible cause of inefficiency. The halo filter was harmless, since it removed identified halo events. From the known rate of beam splashes in the detectors, we estimated that the hit multiplicity filter would lose 0.1% of good events overlapped by random splashes of beam particles. We first analyzed those events rejected because of high multiplicity in S6 and S7. By using the S1, S2 and S3 points,

we projected the antiproton track into S6; the projected point would be the impact point of the elastically scattered proton if the event was elastic. Fig. 11 shows the y vs. x distribution of the projected impact points in S6. Indeed, 73% of the rejected events point to the beam pipe and can be attributed to elastic events out of acceptance. Of the remaining 27% of these events, 18% project inside the detectors and 9% inside the vacuum chamber. In each of the two regions, these events correspond to 3.3% of the elastic events or 15% of the single diffraction proton dissociation events. We investigated the single diffraction hypothesis. In our diffractive analysis [12], we determined that 18% of the single proton diffraction dissociation cross section is at *low masses* (M^2 <6 GeV^2); these masses have predominant 2 and 3 body decays. The decay products, at very small angle with respect to the beam, are likely candidates to produce nuclear interactions in the beam pipe in front of S6. We know from our simulation that 40% of the *low mass* events should also be detected by our inelastic vertex detector around the interaction region and, in fact, 40±6% of the remaining 27% of the events rejected by the hit filter events were detected. For events rejected by the multiplicity filter in S1 and S2, we looked at the collinearity distribution using S3, S6 and S7 (Fig. 12). The comparison with the collinearity distribution of good events shows that ≃0.1% of good elastic events could at most have been rejected, in agreement with the estimated probability of a beam splash overlapping a good event.

C. EVENT LOSSES DUE TO NUCLEAR INTERACTIONS IN THE DETECTORS

Given the thickness of the components of a detector, nuclear interaction losses were calculated to be $\simeq$1.4%. As this correction is not negligible, we checked it using our data. By looking at events which had a single track in the S2 (S6) detector but more than one track in the following S1 (S7) detector, we determined the nuclear loss correction to be 1.2%$\pm$0.1% on the basis of 750 interactions observed in all our data. When the interaction occurred at the end of S2 (S6), hits were always observed in the S1 (S7) detector of the opposite arm; the opposite side was clean when the interaction occurred in S1 (S7). In this last category of events, by projecting from S2, S3 and S6 into S1 and S7, we determined a 45% probability of still finding a track in the right position when a nuclear interaction occurred. These two observations allowed the precise determination of the nuclear interaction losses for elastic and diffractive scattering, as listed in Table 3.

APPENDIX B. GEOMETRICAL ALIGNMENT OF THE SPECTROMETER

The vertical and horizontal coordinate scale were determined by the silicon detector pads and strips, lithographically produced with an accuracy of few μm's over 3.5 cm. For events with only one hit in a given detector, we adjusted the chamber drift velocity by minimizing (x_{drift}-x_{sil}) vs x_{sil} (Fig. 13). The same procedure was used for the delay lines, which required nonlinear corrections at both y-ends of the detector (Fig.

14). Since the silicon pads had better y-resolution than the chambers and were fully efficient, the y-coordinate was determined by the silicon. The y-coordinate scale was known to better than one part in ten thousand (accuracy of the lithographic mask). On the contrary, the x-coordinate was determined by the chambers, which had better x-resolution. Within the available statistics, the absolute x-scale for each detector was determined to two parts in a thousand (70 μ over 3.5 cm). Since the elastic scattering angle was determined by all detectors, the error on the θ_x scale was reduced to less than one part in a thousand.

In order to reduce the x and y-offset of each detector resulting from the survey, we selected events with only one hit in every detector (hits ought to be within a few millimeters from a straight line fit); assuming that these events originated at x=y=z=0 , by using eq. (1) we projected all points in S3 into the other four detectors and corrected for the x and y-offset of each detector by subtracting the mean value of the distribution of the differences between the measured and projected coordinates. Within the statistics, the detectors of each arm were aligned to within 3.0 μm, as shown in Fig. 15. As a by-product, we determined the detector resolutions quoted in section I and used in the simulation. Fig. 16 shows distributions of the difference between the coordinates as measured by S2 (S6) and as projected into S2 (S6) by using S1,S3 and S7, for elastic events selected by S1, S3 and S6 only. As shown from the comparison with simulated events, detector resolutions have a gaussian distribution; therefore, non-gaussian tails in collinearity distributions could only be attributed to background.

Once we aligned independently the two spectrometer arms, we determined the horizontal angle between them by minimizing the sum $\sum_{i=1}^{5}(\Delta d_i)^2$, where Δd_i is the difference between the surveyed and actual distance d_i between two detectors in different arms

at a given z_i-position. After minimization, the standard deviation of Δd_i was about 70 μm, consistent with the survey error; as a consequence, a systematical error of $(\sum_{i=1}^{5}(\frac{L_i^h}{50\mu m})^2)^{-\frac{1}{2}}$=0.5 (1.2) μrad was estimated on the minimum angle detected by the spectrometers at $\sqrt{s}$=546 (1800) GeV.

A second method, independent of the survey, was used to determine the angle between the two spectrometers. In single diffraction events [12], recoil antiprotons with momentum smaller than $\sqrt{s}/2$ were selected which, bent by the dipole string, passed through S1 and S2 in arm-1 and through S3 in either arm. The recoils were projected from S1 and S2 into S3 assuming x=y=0 at z=0. From the mean value of the distribution of the difference between the measured and projected x-coordinates in S3, we determined that the distance between the two spectrometer arms in S3 should be corrected by 2.0±40.0 μm and -1.0±30 μm at $\sqrt{s}$ =546 and 1800 GeV, respectively (see Fig. 17). At $\sqrt{s}$=546 (1800), the two methods described above set a limit of 0.48 (0.36) μrad on the systematical error in the determination of minimum angle detected by the spectrometer.

APPENDIX C. STUDY OF THE TEVATRON MAGNETIC LATTICE

A. $\sqrt{s}$=1800 GeV

At $\sqrt{s}$=1800, only the quadrupole magnets q_1 and q_2 were powered on the spectrometer *west* side. Assuming that all elastic events came from x=y=z=0 and using eq. (1), we

projected the impact point of an elastic recoil scattered at an angle θ from S3 into S2 as follows:

$$x_{2proj} = \frac{L_2^h}{L_3^h} x_3, \quad y_{2proj} = \frac{L_2^v}{L_3^v} y_3$$

We then studied the differences between the projected and measured coordinates in S2 vs. the measured coordinates in S3 for all events, since wrong ratios of the focal lengths $R_{h(v)} = L_2^{h(v)}/L_3^{h(v)}$ would produce a distortion

$$\delta x(y) = x(y)_2 - x(y)_{2proj} = \delta R_{h(v)} \cdot x(y)_3$$

where $\delta R_{h(v)}$ is the error in $R_{h(v)}$. Fig. 18 shows the mean of the $\delta x(y)$ distributions as a function of $x(y)_3$ from the data and simulation; distortion at the boundaries of the S3 detector are due to the detector acceptance. The data and, as a check, an equal number of simulated events were fitted with the form $\delta R_{h(v)} \cdot x(y)_3$. For the data, the quadrupole magnetic strength was changed until $\delta R_{h(v)}$ was found null within our sensitivity. This was achieved by adjusting the q_2 nominal magnetic strength by 2%. Since on the *east* side the magnet q_2 is behind the S6 and S7 detectors, the nominal optics was not changed on this side. The lattice functions were verified by projecting tracks from the *west* into the *east* side. We assigned a 0.48% error to the determination of δR_h, of which 0.12% is statistical, 0.22% is due to our systematical error on the x-scale and the rest was estimated by changing the fit region. The error on δR_v was 0.6%, of which 0.2% statistical and the rest due to the discrete structure of the y-coordinate and the sensitivity to the fit region. As shown in Fig. 19, the ratios R_h and R_v behave differently for changes of the quadrupole strengths and therefore allow

the determination of the q_1 magnetic strength; the uncertainties on $R_{h(v)}$ contribute a 1.0% error in the determination of the q_1 magnetic strength. By changing q_1 by this amount, the focal lengths in S3 and S6 change by 0.15% in the horizontal plane and 0.2% in the vertical plane. Inserting these focal length changes in the simulation, we derived a systematical error of 0.2% in the determination of the optical point, 0.1% on the elastic slope and 0.3% on the total elastic rate.

B. $\sqrt{s}$=546 GeV

At $\sqrt{s}$=546, the Tevatron magnetic field, well known at full power, was reduced by a factor three. We first took test data with the q_0 magnet string powered off and checked that remnant field distortions in q_1 and q_2 were not appreciable. During the data taking, the quadrupole magnets q_0 were powered. We repeated the previous study by changing the strength of all q_0 quadrupoles by the same amount. This time the distortion was defined as

$$\delta x(y) = x(y)_3 - x(y)_{3proj} = \delta R_{h(v)} \cdot x(y)_2$$

where $R_{h(v)} = \frac{L_3^{h(v)}}{L_2^{h(v)}}$. The q_0's strength was adjusted by 0.8%. The uncertainty on δR_h was estimated to be 0.48% (Fig. 20), while δR_v could not be determined to better than 4.0% because of the limited y-range covered by S2. As shown in Fig. 21, the $\delta R_{h(v)}$ accuracy corresponds to an uncertainty on the q_0's strength of 0.2%. By changing the q_0's strength by such an amount in the simulation, we derived a systematic error of 0.4% in the determination of the optical point, 0.1% on the slope and 0.4% on the total elastic rate.

C. DETERMINATION OF THE BEAM POSITION WITH RESPECT TO THE CENTER OF THE TEVATRON MAGNETIC LATTICE

The spectrometer detectors were surveyed with respect to the Tevatron magnetic axis with an accuracy of 0.1 mm. With our alignment procedure, we corrected the detector positions for 0.1 mm offsets, working in the beam reference system. However, we noticed that, although in all three runs (two at $\sqrt{s}$=546 and one at $\sqrt{s}$=1800) the detectors were placed at about the same distance from the beam, the actual positions relative to the nominal beam axis differed by several millimetres among runs, indicating that the beam position (X_0,Y_0) at z=0 and the beam angle (Θ_{0x}, Θ_{0y}) in the magnetic lattice frame were different in every run. The beam position with respect to the magnetic axis was determined for every run using the data. In the beam-axis reference system, for a given run r, we define x^r_{0i}, y^r_{0i}, x^r_{1i} and y^r_{1i} as the coordinates of the center of each detector Si in arm-0 and arm-1, respectively. In the survey reference system, the centre of each detector Si in the spectrometer arm-j has coordinates x'^r_{ji} and y'^r_{ji}, and, for all runs, the same offsets δx^j_i and δy^j_i with respect to the magnetic lattice axis. Therefore, in the magnetic lattice reference system, the detector coordinates are

$$x''^r_{ji} = x'^r_{ji} + \delta x^j_i = x^r_{ji} + X^r_0 \varepsilon^{hr}_i + L^{hr}_i \Theta^r_{0x}$$

$$y''^r_{ji} = y'^r_{ji} + \delta y^j_i = y^r_{ji} + Y^r_0 \varepsilon^{vr}_i + L^{vr}_i \Theta^r_{0y}$$

where (ε^r_i, L^r_i) are the transport matrix coefficients listed in Table 1. For two different runs r and s, the quantities

$$\Delta^{rs}_{ji} = x'^r_{ji} - x'^s_{ji} - x^r_{ji} + x^s_{ji}$$

$$\Omega_{ji}^{rs} = y_{ji}^{'r} - y_{ji}^{'s} - y_{ji}^{r} + y_{ji}^{s}$$

were known from survey and alignment with the data to better than 100 μm. We fitted all Δ_{ji}^{rs} and Ω_{ji}^{rs} values derived from all combinations of runs with the forms

$$\varepsilon_i^{hr} X_0^r - \varepsilon_i^{hs} X_0^s + L_i^{hr} \Theta_{0x}^r - L_i^{hs} \Theta_{0x}^s$$

$$\varepsilon_i^{vr} Y_0^r - \varepsilon_i^{vs} Y_0^s + L_i^{vr} \Theta_{0y}^r - L_i^{vs} \Theta_{0y}^s$$

where the beam angle Θ_0^r and position (X_0^r,Y_0^r) in each run r were fit parameters. We derived Y_0=0.0 within 0.2 mm and Θ_{0Y}=0 within 3 μrad in all runs. In the x-z magnetic lattice plane, we obtained

Run	X_0 (cm)	Θ_{0x} (μrad)
$\sqrt{s}$=546	0.1±0.05	27.0±2.6
1^{st} at $\sqrt{s}$=1800	0.02±0.01	-8.0±2.0
2^{nd} at $\sqrt{s}$=1800	-0.25±0.01	7.0±2.0

This determination of the beam angle and position for each run was important for obtaining a momentum resolution better than 0.2% for the diffractive antiproton recoils with momentum smaller than that of the beam.

APPENDIX D. MONTE CARLO SIMULATION

Neglecting detector resolution and beam dispersion at the interaction point, the spectrometer acceptance α is function of the four momentum transfer $t = -p^2\theta^2$:

$$\alpha = \begin{cases} 0 & \text{if } 0.0 < -t < (p\theta_x^{min})^2 \\ \frac{1}{\pi}\cos^{-1}(\frac{\theta_x^{min}p}{\sqrt{-t}}) & \text{if } (p\theta_x^{min})^2 < -t < (p\theta_c)^2 \\ \frac{1}{\pi}\sin^{-1}(\frac{\theta_y^{max}p}{\sqrt{-t}}) & \text{if } (p\theta_c)^2 < -t < (p\theta_c')^2 \\ \frac{1}{\pi}[\sin^{-1}(\frac{\theta_y^{max}p}{\sqrt{-t}}) - \cos^{-1}(\frac{\theta_x^{max}p}{\sqrt{-t}})] & \text{if } (p\theta_c')^2 < -t < (p\theta_x^{max})^2 \\ 0 & \text{if } (p\theta_x^{max})^2 < -t \end{cases} \quad (2)$$

where p is the beam momentum, θ is the elastic scattering angle, $\theta_c = \sqrt{(\theta_x^{min})^2 + (\theta_y^{max})^2}$ and $\theta_c' = \sqrt{(\theta_x^{max})^2 + (\theta_y^{max})^2}$. The angles $\theta_x^{max(min)}$ and θ_y^{max} are the smallest (largest) of the maximum (minimum) angles $\mathrm{x}_i^{max(min)}/L_i^h$ and y_i^{max}/L_i^v covered by the detectors Si. The Monte Carlo simulation incorporates the smearing effect of the detector resolution and of the beam dispersion at the interaction point. In the simulation, the beam profile and angular dispersion at the interaction region were assumed to be gaussian distributions with $\sigma_{x,y}$ and $\sigma_{\theta_{x,y}}$ as determined by flying wire measurements of the beam emittance during the runs (see Table 8). As shown in Fig. 22, the geometrical acceptances compare well to the ones derived by the complete simulation at $\sqrt{s}$=546 and 1800 GeV, indicating that smearing effects are small. Fig. 23 compares the interaction point and collinearity distributions for data and simulation at $\sqrt{s}$=1800 GeV. At the same energy, Fig. 24 compares x and y-distributions measured by all detectors and projected at the z-position of S6 in each spectrometer arm for the data and for an equal number of simulated events.

References

[1] G. Apollinari et al.,"The Small Angle Spectrometer of CDF", N.I.M. A289 (1990) 375

[2] G. Apollinari et al., "Two Dimensional Tracking with Surface Barrier Silicon Detectors", IEEE Trans. on Nucl. Sci. 36 (1989) 46

[3] R. Johnson, "Absolute Luminosity and Energy Determination in Bunched Colliding Beam Machines", Proceedings of the CERN-USA Accelerator School, Capri, 1988

[4] R.Castaldi and G.Sanguinetti, "Elastic Scattering and Total Cross Section at Very High Energy", Ann. Rev. Nucl. Part. Sci. (1985) 351

[5] R.Cahn, "Coulombic-Hadronic Interference in an Eikonal Model ", Zeitschr. fuer Phys. C15 (1982) 253

[6] M. Bozzo et al., The UA4 Collaboration, "Low Momentum Transfer Elastic Scattering at the CERN Proton-Antiproton Collider", Phys. Lett. 147B (1984) 385

[7] M. Bozzo et al., The UA4/2 Collaboration, "Measurement of the Real Part of the $\bar{p}p$ Scattering Amplitude at the CERN SPS Collider", Results and Perspectives in Part. Phys., La Thuile (1993)

[8] N.M. Amos et al., " Measurement of ρ, the Ratio of the Real to Imaginary Part of the $\bar{p}p$ Forward Elastic Scattering Amplitude, at $\sqrt{s}$=1.8 TeV", Phys. Rev. Lett. 68 (1992) 2433

[9] The CDF Collaboration , "Measurement of the Antiproton-Proton Total Cross Section at $\sqrt{s} = 546$ and $\sqrt{s} = 1800$ GeV".

[10] D.S. Ayres et al., "$\pi^{\pm}$, $K^{\pm}$, pp and $p\bar{p}$ Elastic Scattering from 50 to 175 GeV/c", Phys. Rev. D 15 (1977) 3107

[11] M. Ambrosio et al., "Measurement of the Elastic Scattering in $p\bar{p}$ Collisions at 52.8 C.M. Energy", Phys. Lett. 115B (1982) 495

N.Amos et al., "Comparison of Small-Angle $\bar{p}p$ and pp Elastic Scattering at 52.8 GeV C.M. Energy at the CERN ISR", Phys. Lett. 120B (1983) 460

N.Amos et al., "Comparison of Small-Angle $\bar{p}p$ and pp Elastic Scattering at the CERN ISR", Phys. Lett. 128B (1983) 343

[12] The CDF Collaboration ,"Measurement of $\bar{p}p$ Single Diffraction Dissociation at $\sqrt{s} = 546$ and $\sqrt{s} = 1800$ GeV".

Table 1: Transport matrix elements

		$\sqrt{s}$=546				$\sqrt{s}$ =1800			
z (cm)		ε^h	L^h (cm)	ε^v	L^v (cm)	ε^h	L^h (cm)	ε^v	L^v (cm)
5849.0	S1	-0.524	1719.8	-2.861	982.0	1.204	5698.8	0.077	4029.7
5544.2	S2	-.404	1918.3	-2.542	981.8	1.224	5533.8	0.150	3827.5
3122.0	S3	0.478	3019.7	-0.126	1115.4	1.197	3667.7	0.810	2597.0
-3089.3	S6	-.099	-1131.3	0.484	-2989.0	0.829	-2615.4	1.178	-3581.3
-3182.4	S7	-0.177	-1086.0	0.467	-3076.4	0.777	-2562.9	1.233	-3827.1

Table 2: Analysis event flow

	$\sqrt{s}$=546	1^{st} run at $\sqrt{s}$=1800	2^{nd} run at $\sqrt{s}$=1800
	number of events		
Triggers	34522	16993	21766
TOF filter	33714	15493	19126
HALO filter	33714	11402	16167
HIT filter	29981	8692	13054
ROAD filter	28151	6136	8055
Vertex cut	23868	5313	7033
Collinearity cut	22929	4856	6662
Fiducial cut	18919	3144	5630

Table 3: Corrections (%)

	$\sqrt{s}$=546	1^{st} run at $\sqrt{s}$=1800	2^{nd} run at $\sqrt{s}$=1800
	arm-0/arm-1	arm-0/1	arm-0/1
Background	-0.3 / -2.2	-0.37 / -0.85	-0.28 / -0.14
TOF losses	+1.1 / +1.65	+1.5 / +1.8	+1.7 / +0.9
Nuclear Interactions	+1.8	+1.8	+1.8
Slope change at $-t > 0.1$ GeV^2 *	+0.78	0	0

* This correction was applied only to the total elastic rate

Table 4: Elastic events (%)

Reconstructed with	$\sqrt{s}$=546	$\sqrt{s}$=1800
5 detectors	95.33	95.25
4 detectors*	4.60	4.70
3 detectors	0.07	0.05
2 detectors	0.00	0.00

* 3.0 are due to nuclear interactions in front of S1, S2, S6 and S7

Table 5: Elastic events (%)

Number of reconstructed elastic combinations at $\sqrt{s}$=546	Number of detectors with more than one hit					
	0	1	2	3	4	5
1	80.05	14.43	1.68	0.21	0.11	0.85
2		1.35	0.41	0.06	0.07	0.14
3		0.32	0.12	0.02	0.01	0.01
>3		0.01	0.11	0.01	0.02	0.01
at $\sqrt{s}$=1800	0	1	2	3	4	5
1	76.87	16.97	2.36	0.28	0.03	
2		1.53	0.48	0.12	0.01	0.01
3		0.39	0.17	0.05	0.00	
>3		0.21	0.49	0.02	0.01	

Table 6: Systematical errors (%)

	$\sqrt{s}$=546			$\sqrt{s}$=1800		
	A	b	N_{el}	A	b	N_{el}
Vertex cut	0.2		0.2	0.2		0.2
TOF losses	0.2		0.2	0.2		0.2
Background	0.2		0.2	0.2		0.2
Magnetic lattice	0.2	0.1	0.2	0.1	0.2	0.3
t_{min}	0.07		0.07	0.17		0.17
x-scale	0.1	0.1		0.1	0.1	
Tilt-angle	0.07	0.05	0.05	0.2	0.07	0.15
Nuclear interactions	0.2		0.2	0.2		0.2
Beam momentum	0.24	0.24		0.24	0.24	
b at $-t$ >0.25 GeV^2						0.2
Total	0.52	0.26	0.45	0.48	0.32	0.54

Table 7: Results

	$\sqrt{s}$=546	$\sqrt{s}$=1800
	Fit results	
b (GeV^{-2})	15.35 $\pm$ 0.19	16.98 $\pm$ 0.24
A (GeV^{-2})	4043598 $\pm$48558	1336532 $\pm$ 40719
(A,b) covariance	0.79	0.93
χ^2	13.06	60.96
N_{DF}	13	46
χ^2/N_{DF}	1.01	1.32
	Final results (systematical errors included)	
L (mb^{-1}) [9]	20625$\pm$2.1%	3939$\pm$3.3%
b (GeV^{-2})	15.35 $\pm$ 0.19	16.98 $\pm$ 0.25
A (GeV^{-2})	4043598$\pm$52915	1336532$\pm$40943
Elastic Rate	265535$\pm$2411	78691$\pm$1463
σ_{el} (mb)	12.9$\pm$0.3	20.0$\pm$0.9
$\frac{d\sigma_{el}}{dt}\|_{t=0}$ (mb$\cdot$GeV^{-2})	196.1$\pm$5.7	339.3$\pm$19.3

Table 8: Beam parameters at the interaction point

$\sqrt{s}$	σ_{X_0}	σ_{Y_0}	$\sigma^p_{\Theta_x}$	$\sigma^{\bar{p}}_{\Theta_x}$	$\sigma^p_{\Theta_y}$	$\sigma^{\bar{p}}_{\Theta_y}$
	(μm)			(μrad)		
546	260.0	190.0	36.4	36.4	31.5	31.5
1800 (1^{st} run)	290.0	200.0	6.0	4.0	6.0	4.0
1800 (2^{nd} run)	250.0	250.0	2.9	3.2	2.9	3.2

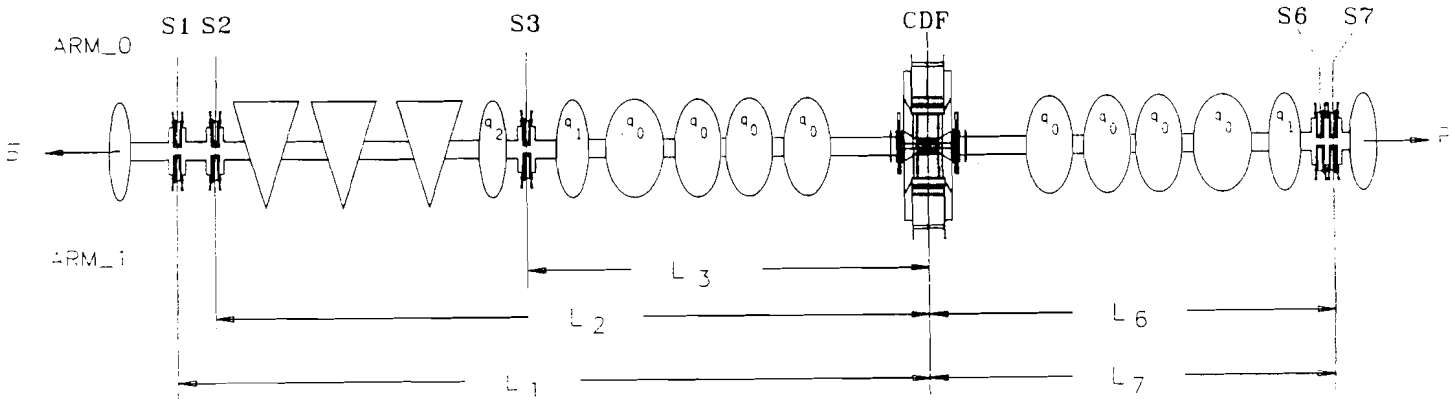

Figure 1: Top view of the elastic scattering set up. Values of the focal lengths L_i are listed in Table 1.

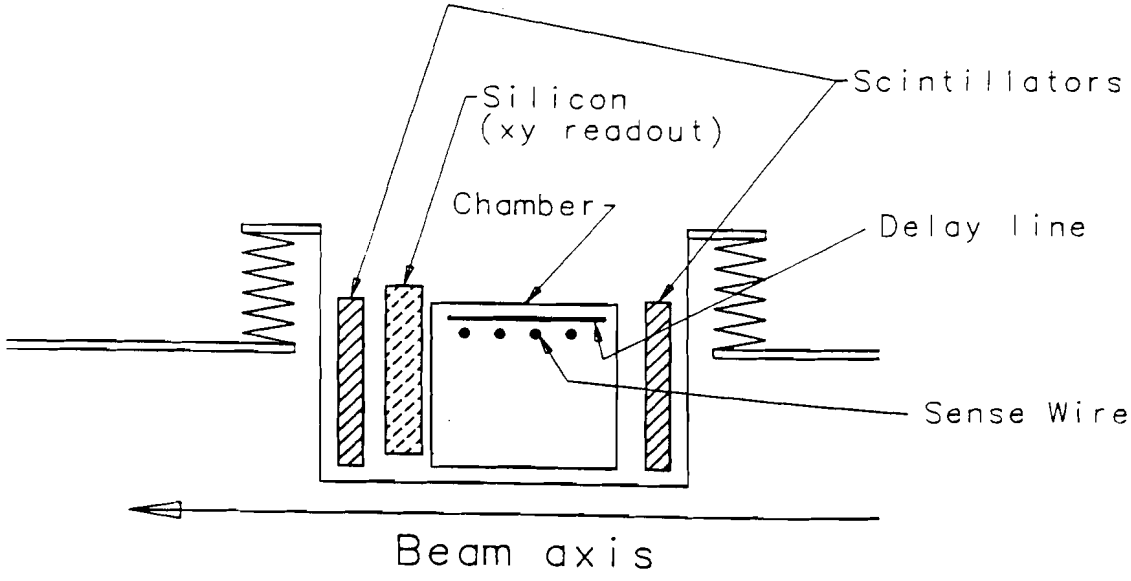

Figure 2: Sketch of a detector assembly (top view); the detector section symmetric with respect to the beam-axis is not shown.

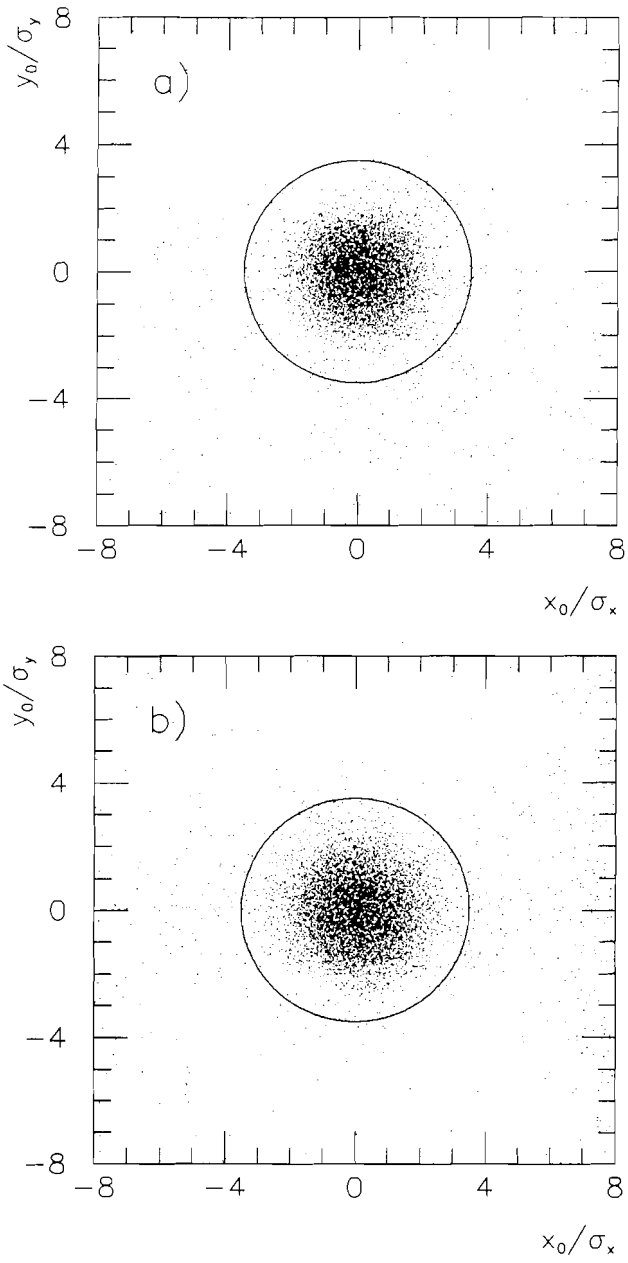

Figure 3: Interaction point distributions in the transverse plane at z=0 for (a) $\sqrt{s}$=546 and (b) $\sqrt{s}$=1800 GeV, in units of the reconstruction errors $\sigma_{x(y)}$ ($\simeq 350\mu$m). The circle indicates the vertex cut.

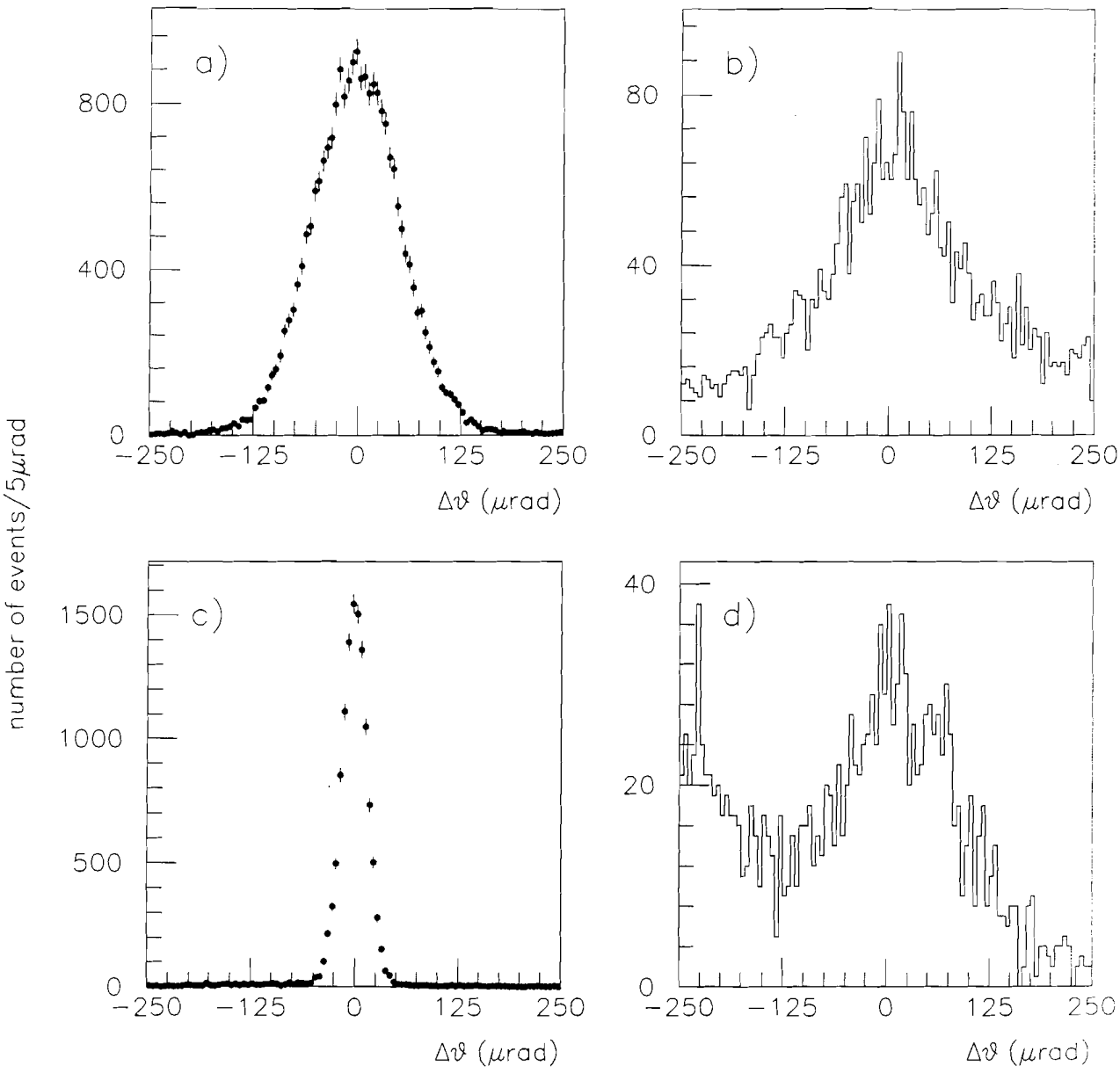

Figure 4: Collinearity ($\Delta\theta = \theta^{\bar{p}} - \theta^{p}$) distributions for (a) events accepted and (b) events rejected by the vertex cut at $\sqrt{s}$=546; (c) and (d) are the corresponding distributions at $\sqrt{s}$=1800 GeV.

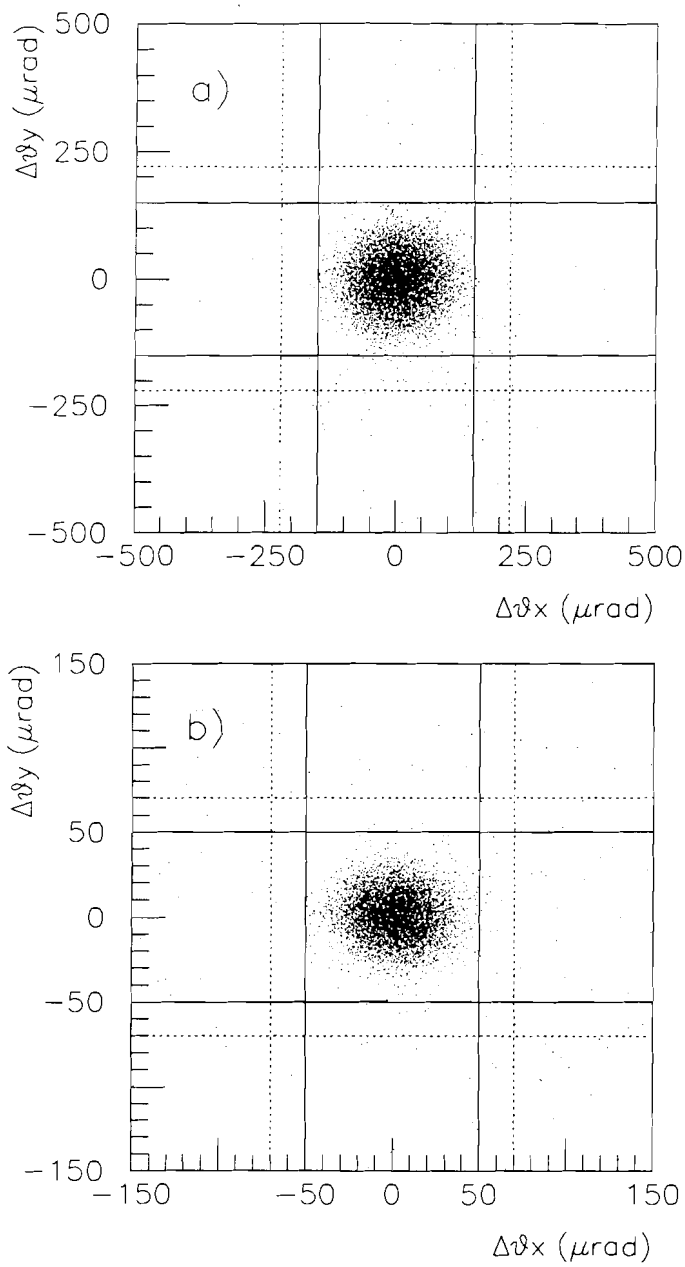

Figure 5: Collinearity distributions ($\Delta\theta_y = \theta_y^{\bar{p}} - \theta_y^p$ vs. $\Delta\theta_x = \theta_x^{\bar{p}} - \theta_x^p$) for events accepted by the vertex cut at (a) $\sqrt{s}$=546 and at (b) $\sqrt{s}$=1800 GeV. The solid lines indicate our collinearity cuts; events with $\Delta\theta_x$ outside the dashed lines are used to estimate the background contamination inside the collinearity cuts.

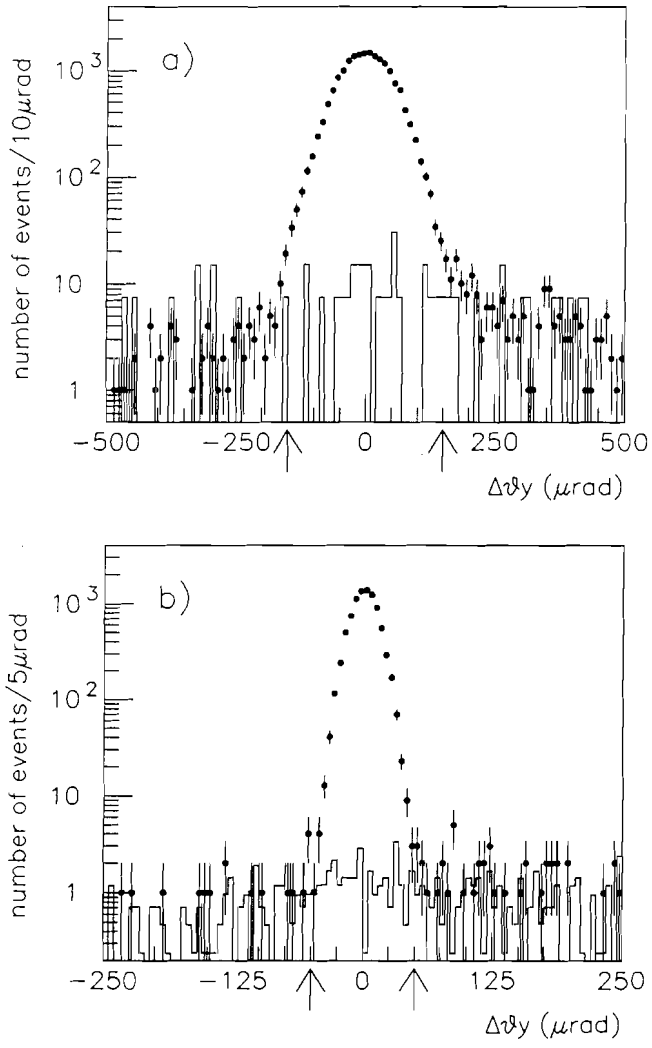

Figure 6: Collinearity ($\Delta\theta_y = \theta_y^{\bar{p}} - \theta_y^{p}$) distributions at (a) $\sqrt{s}$=546 and at (b) $\sqrt{s}$=1800 GeV. The collinearity resolution $\sigma_{\Delta\theta_y}$ is $\simeq$ 50 (12) μrad at $\sqrt{s}$=546 (1800). (•) Events that passed the vertex and the three $\sigma_{\Delta\theta_x}$ collinearity cuts. (—) Background events that passed the vertex cut but have $|\Delta\theta_x| > 4\ \sigma_{\Delta\theta_x}$, normalized to the number of events with $|\Delta\theta_y| > 4\ \sigma_{\Delta\theta_y}$. Arrows indicate the $\Delta\theta_y$ collinearity cut.

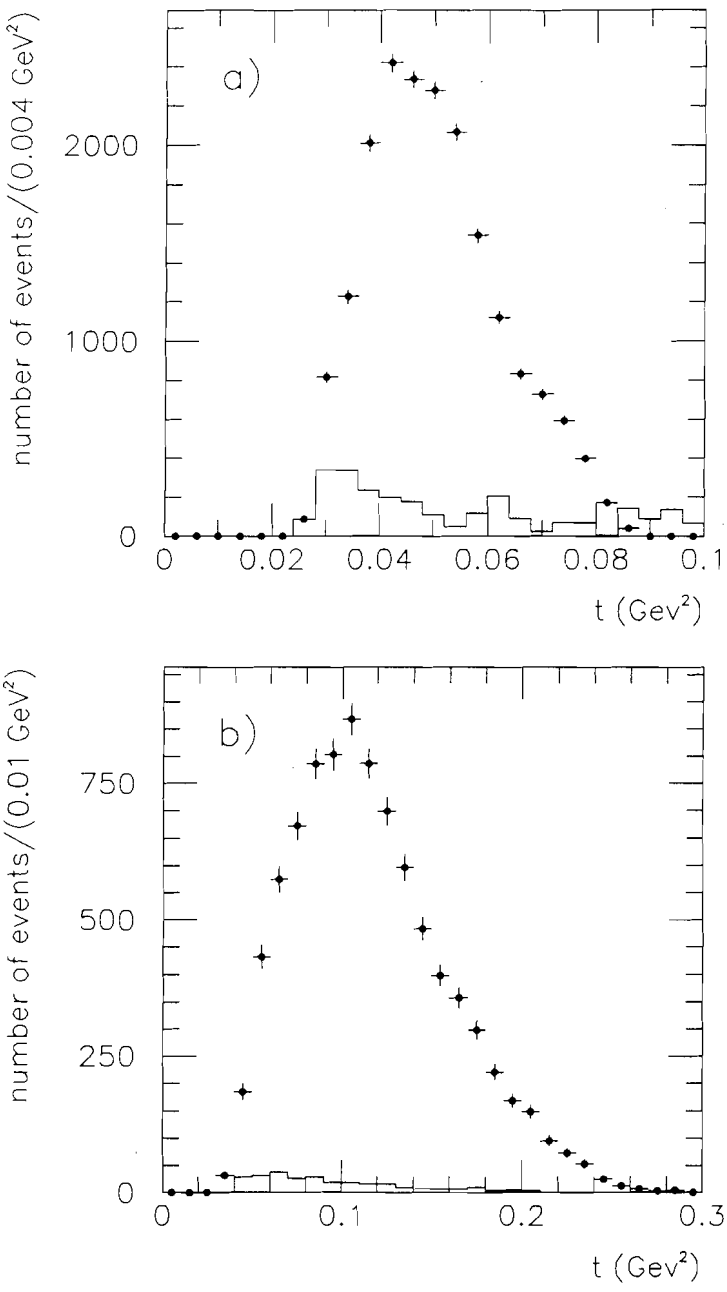

Figure 7: t-distributions for events passing all cuts (•) at (a) $\sqrt{s}$=546 and at (b) $\sqrt{s}$=1800 GeV. The t-distribution of background events passing all cuts (—) is amplified by a factor 10.

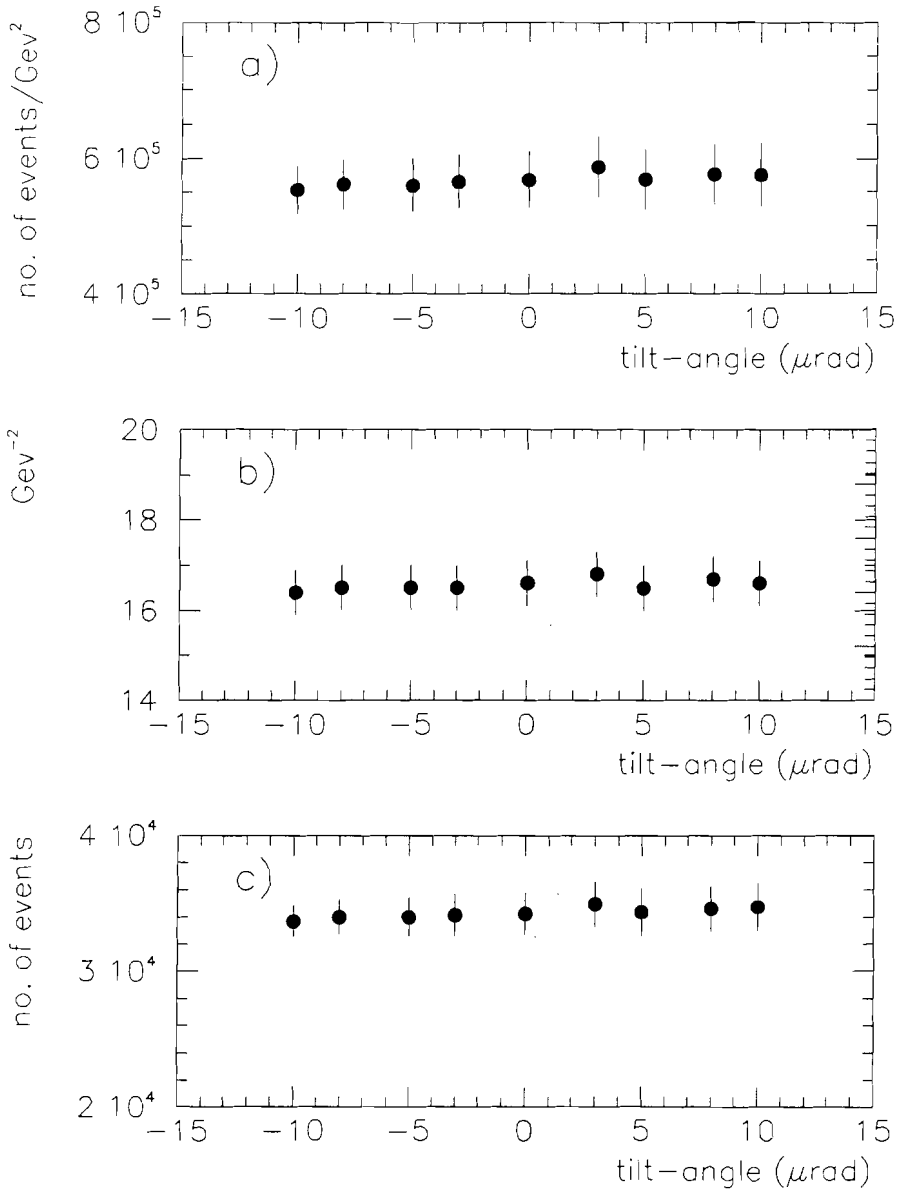

Figure 8: Results of simultaneous fits to the data t-distributions measured by the spectrometer arm-0 and arm-1 as a function of the beam angle with respect to the spectrometer-axis (tilt-angle). For each tilt-angle, t-distributions were corrected for the corresponding acceptance. Data are from the 2^{nd} run at $\sqrt{s}$=1800. (a) Optical point $\frac{dN_{el}}{dt}|_{t=0}$; (b) slope b; (c) number of elastic events, N_{el}.

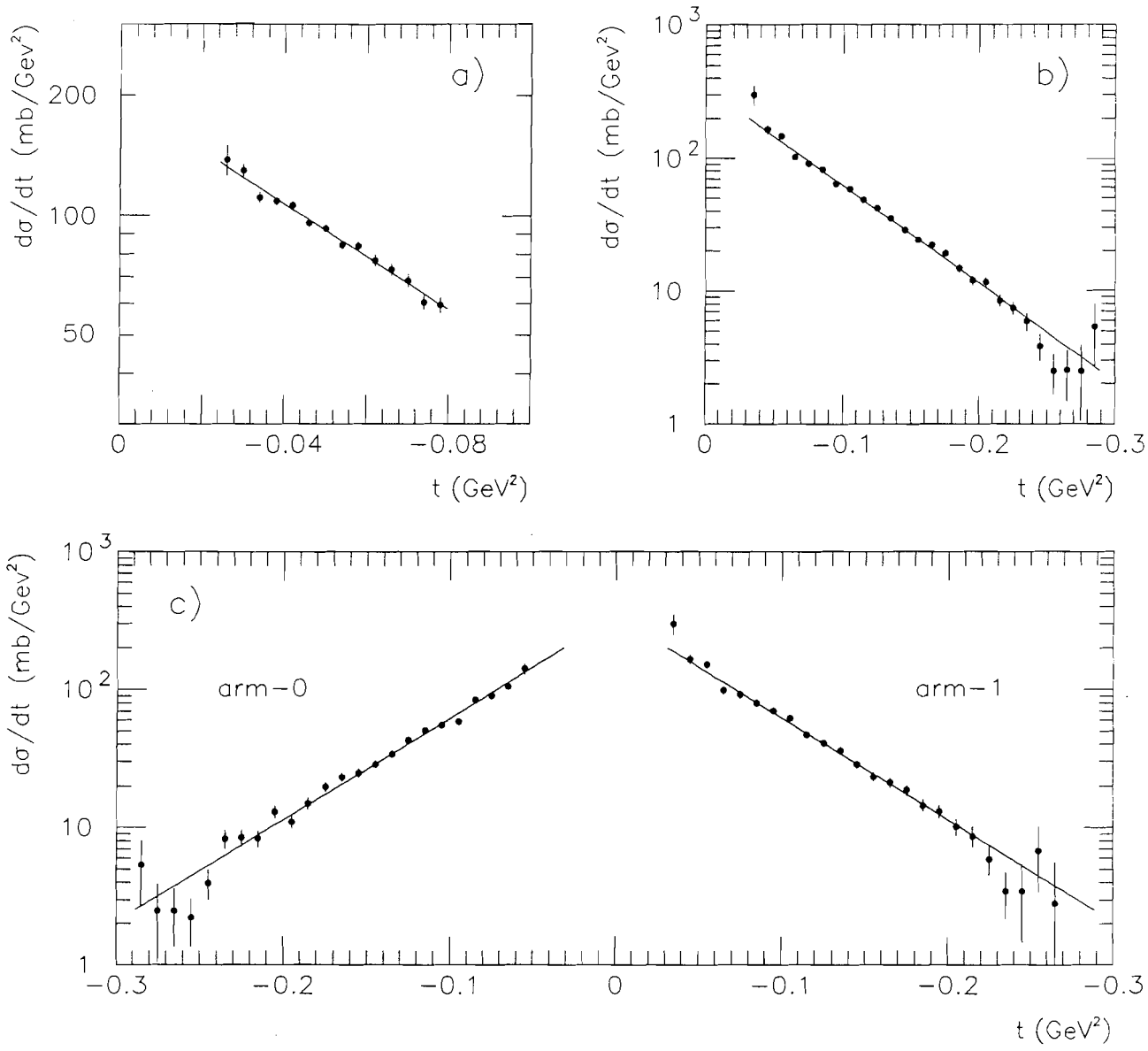

Figure 9: Differential cross section of proton-antiproton elastic scattering at (a) $\sqrt{s}$=546 GeV and at (b) $\sqrt{s}$=1800 GeV; (c): differential cross section measured by each spectrometer arm at $\sqrt{s}$=1800 GeV. Lines represent the fit results described in the text.

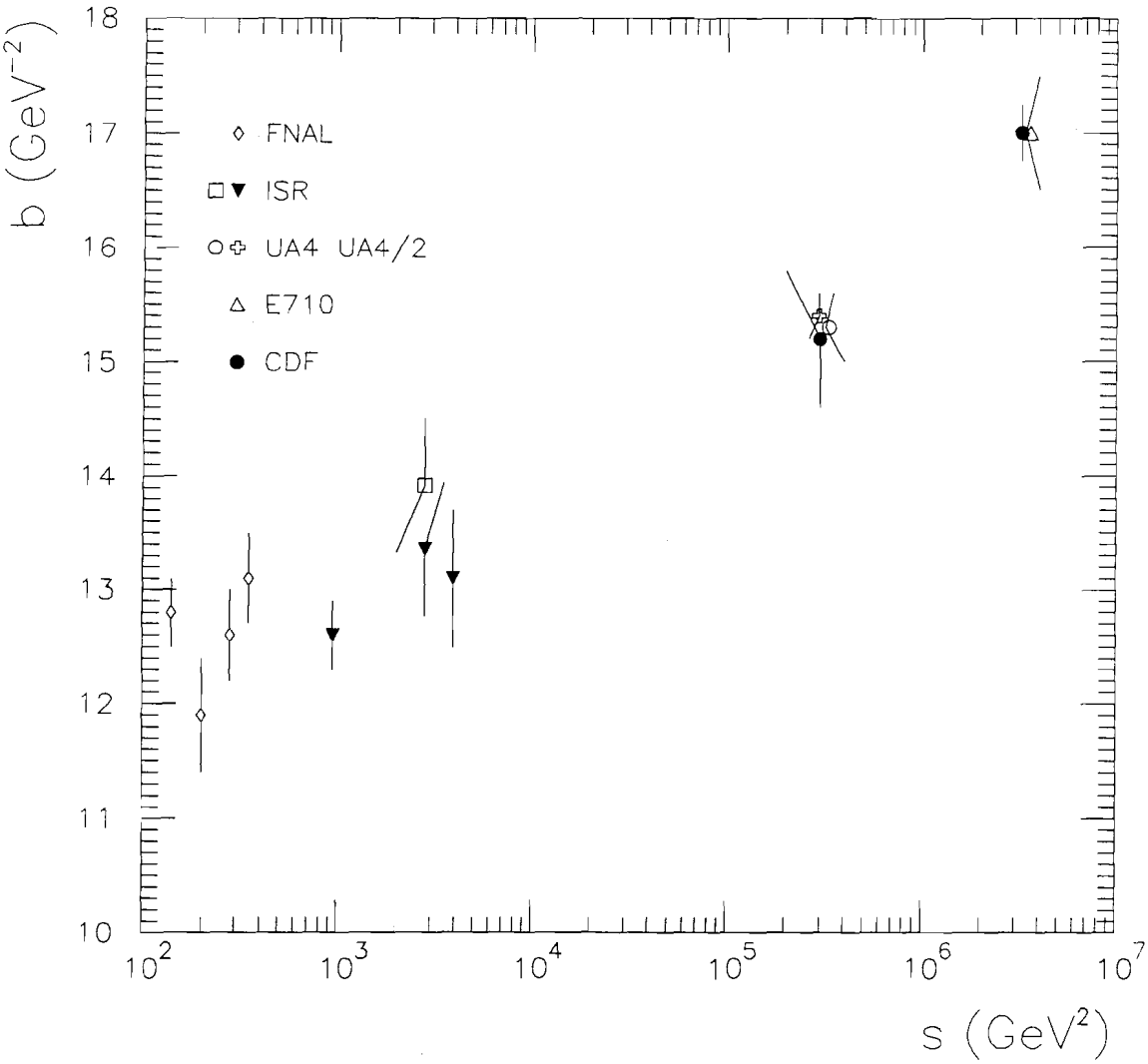

Figure 10: Our results for the slope b compared to other proton-antiproton experiments in a similar t-range ($-t \leq 0.1$ GeV^2): FNAL Ref.[10], ISR Ref.[11], UA4 Ref.[6], UA4/2 Ref. [7], E710 Ref.[8].

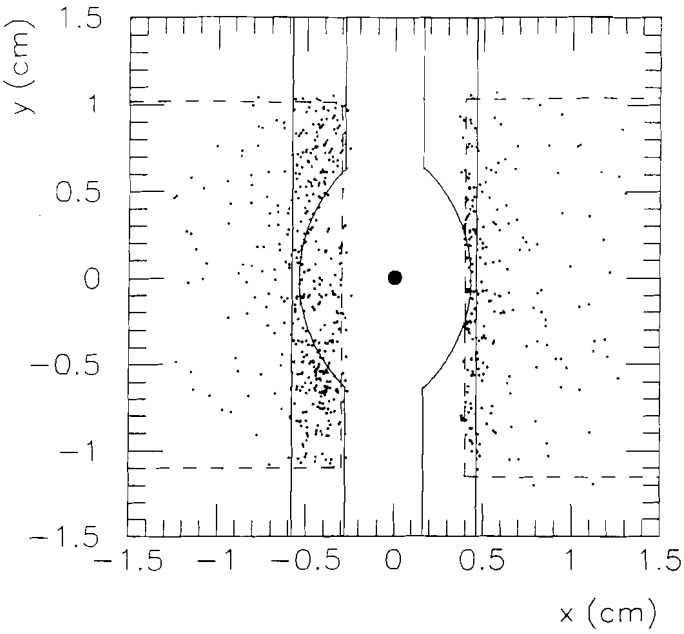

Figure 11: Impact point distribution obtained by projecting the antiproton tracks onto detector S6 (on the proton side) for events rejected because of many hits in S6+S7 (HIT FILTER) at $\sqrt{s}$=1800 GeV. The solid line indicates the beam pipe; (− − −) acceptance of the antiproton detectors projected in S6; (•) beam position.

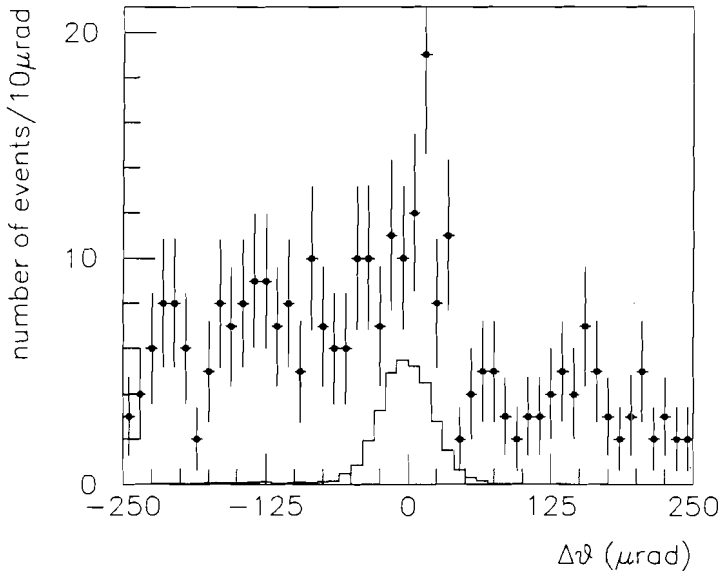

Figure 12: Collinearity ($\Delta\theta = \theta^{\bar{p}} - \theta^{p}$) distribution (•) for events rejected because of large multiplicities in S1+S2 (HIT FILTER) in all the data (corresponding to 27693 good elastic events), after the fiducial and vertex cuts. The solid line shows the collinearity distribution of elastic events.

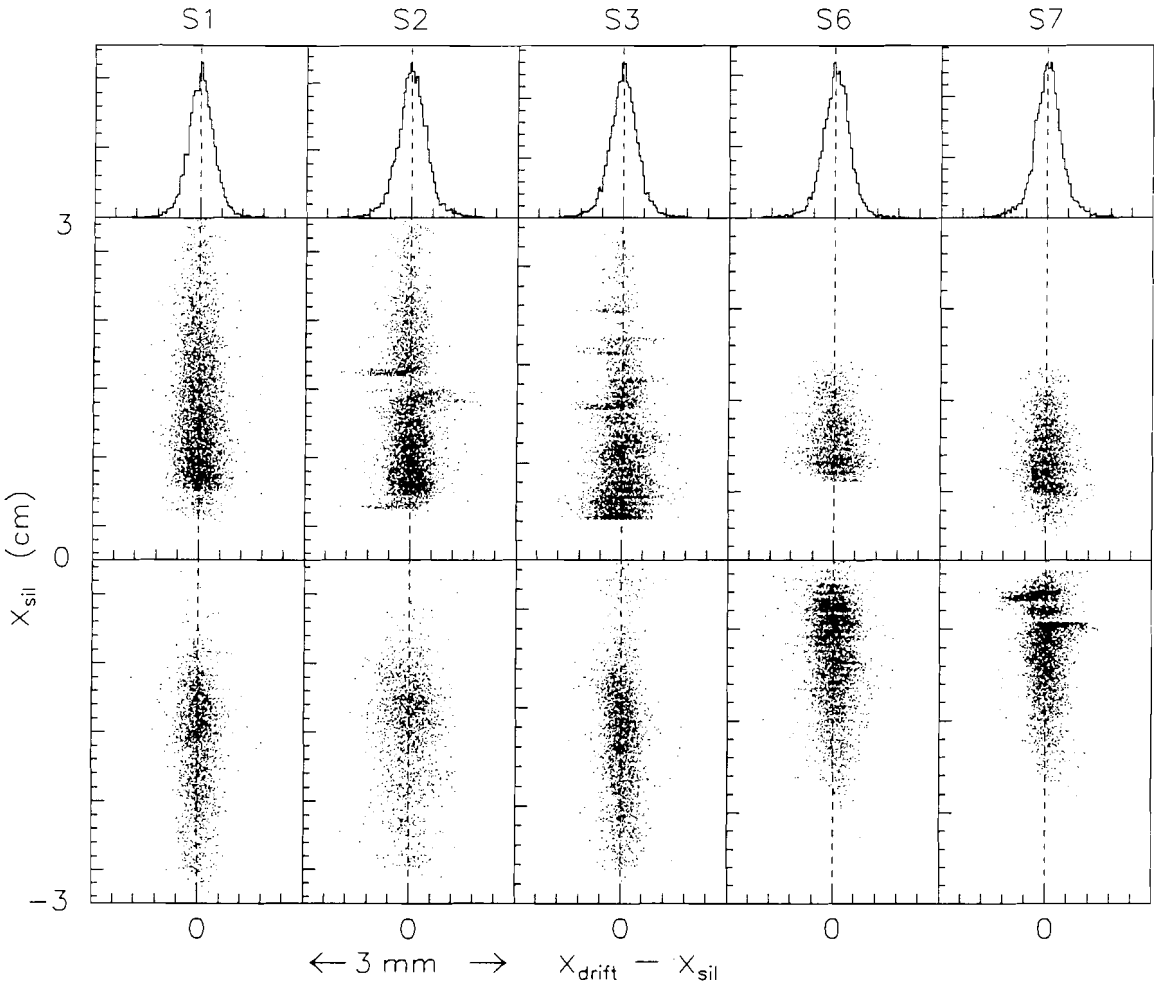

Figure 13: Distribution of the difference between the x-coordinate measured by the drift chamber (x_{drift}) and by the silicon (x_{sil}) vs. x_{sil} for each spectrometer detector at $\sqrt{s}$=1800 GeV.

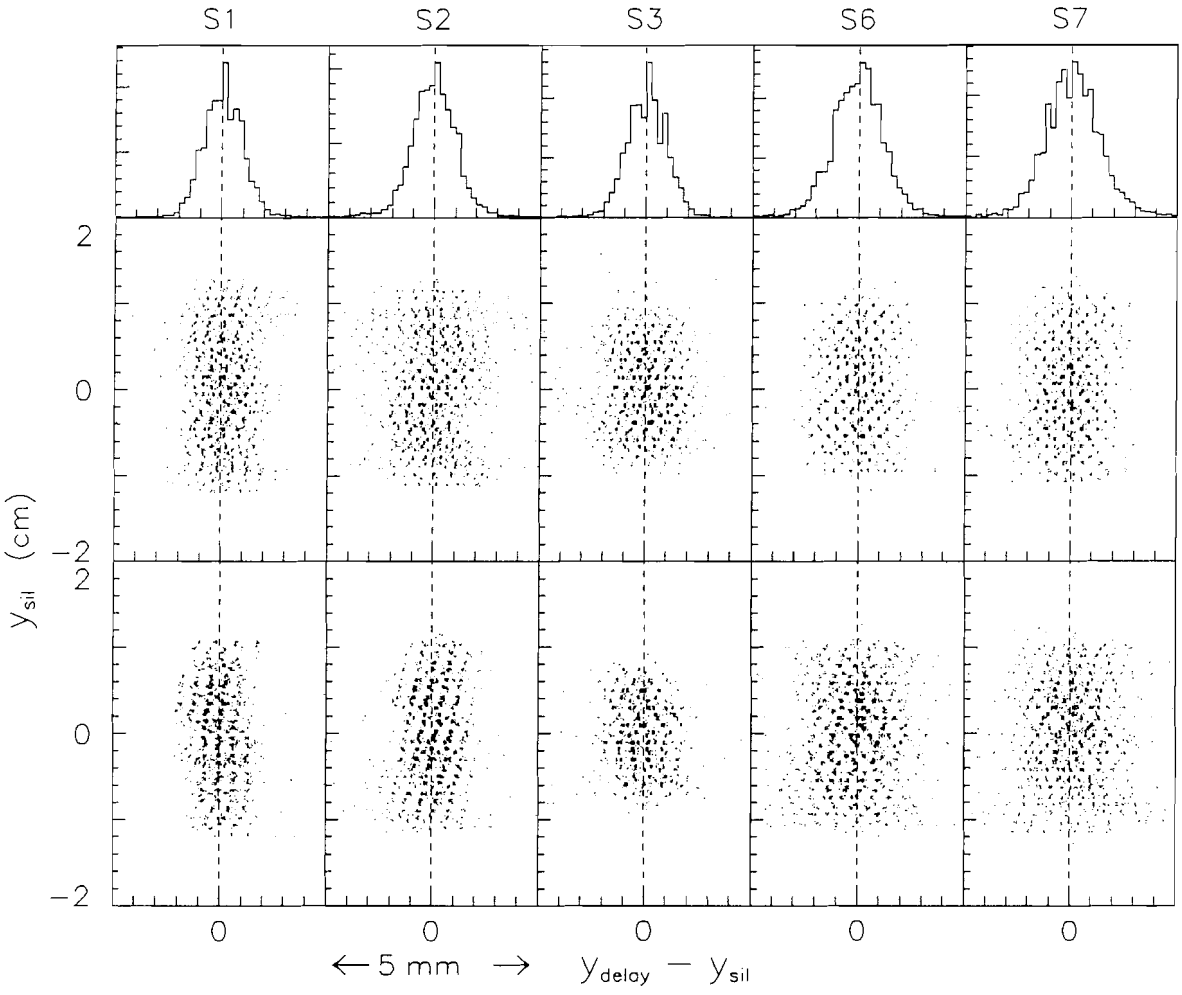

Figure 14: Distribution of the difference between the y-coordinate measured by the delay line (y_{delay}) and by the silicon (y_{sil}) vs. y_{sil} for each spectrometer detector at $\sqrt{s}$=1800 GeV.

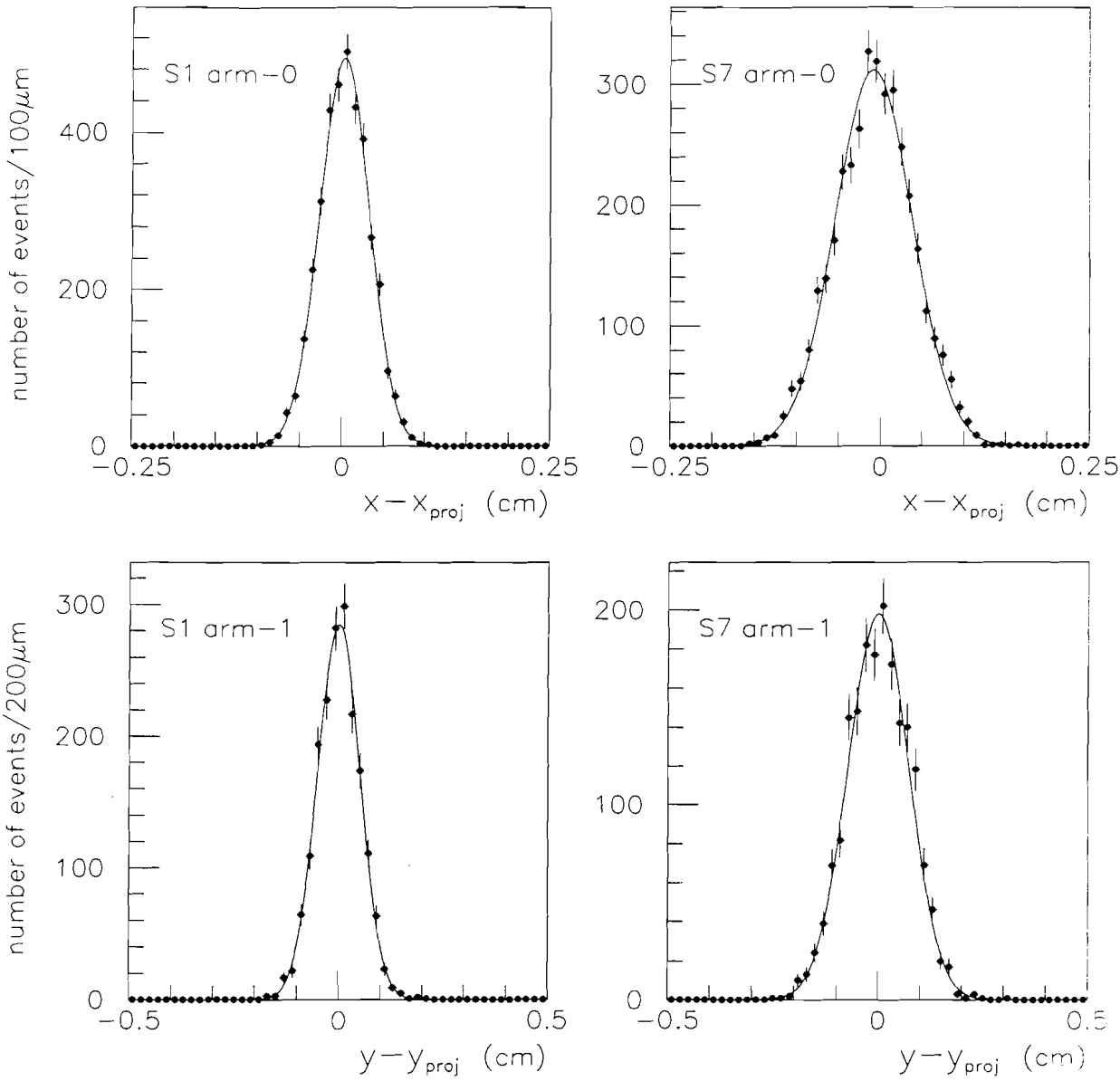

Figure 15: Typical distributions of the difference between the coordinate measured by detectors S1 and S7 and the projected value, calculated using the coordinates measured by S3 and assuming the interaction point to be at (x,y,z)=(0,0,0). The data are at $\sqrt{s}$=1800. The distribution mean values have been adjusted to the offsets (($\simeq$ 20μm) predicted by the simulation when assuming a point-like interaction region. Solid lines represent gaussian fits to the distributions.

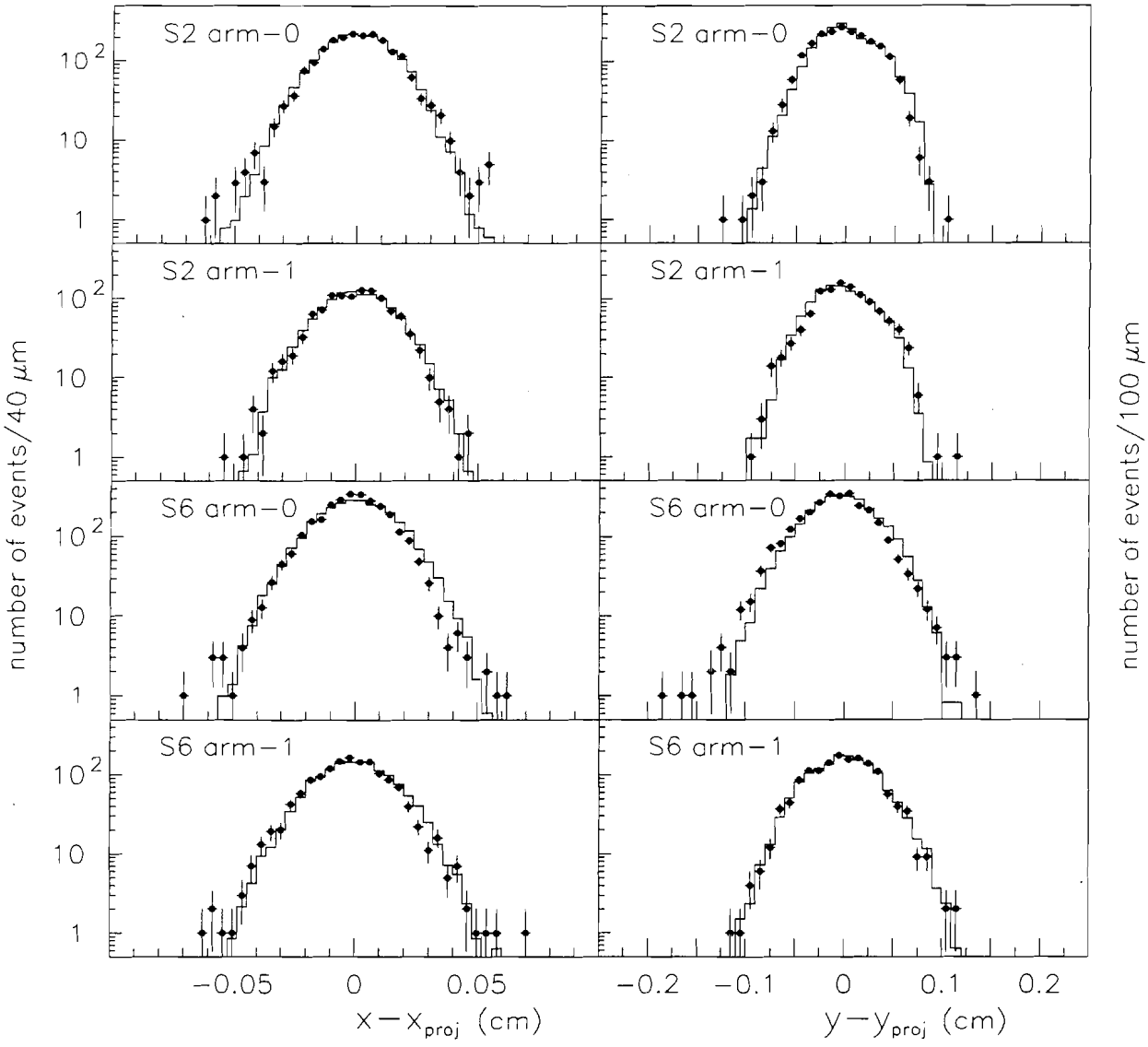

Figure 16: Distributions of the difference between the coordinate measured by detectors S2 and S6 and the projected value, calculated using the coordinates measured by S1, S3 and S7. (•) Data are at $\sqrt{s}$=1800 GeV; (—) equal number of simulated elastic events.

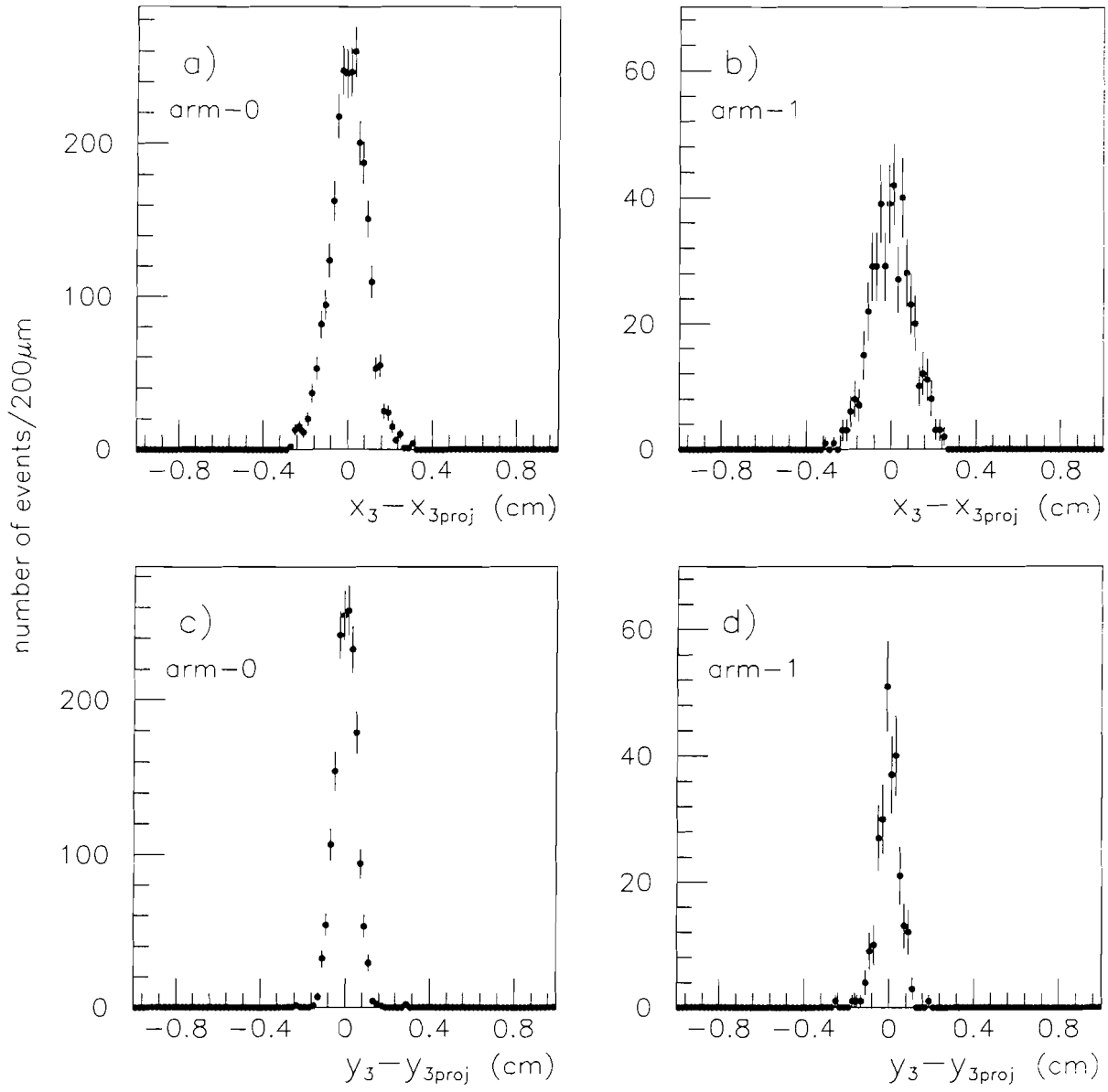

Figure 17: Distributions of the difference between the coordinate measured by the detector S3 and the projected value, calculated using the coordinates measured by S1, S2 and assuming the interaction point at (x,y,z)=(0,0,0) for the recoil antiproton in single diffraction events. S1 and S2 are are always in arm-1, while S3 is in arm-0 or arm-1 depending on the recoil momentum and angle. (a,b) $\sqrt{s}$ = 546 GeV; (c,d) $\sqrt{s}$ = 1800 GeV.

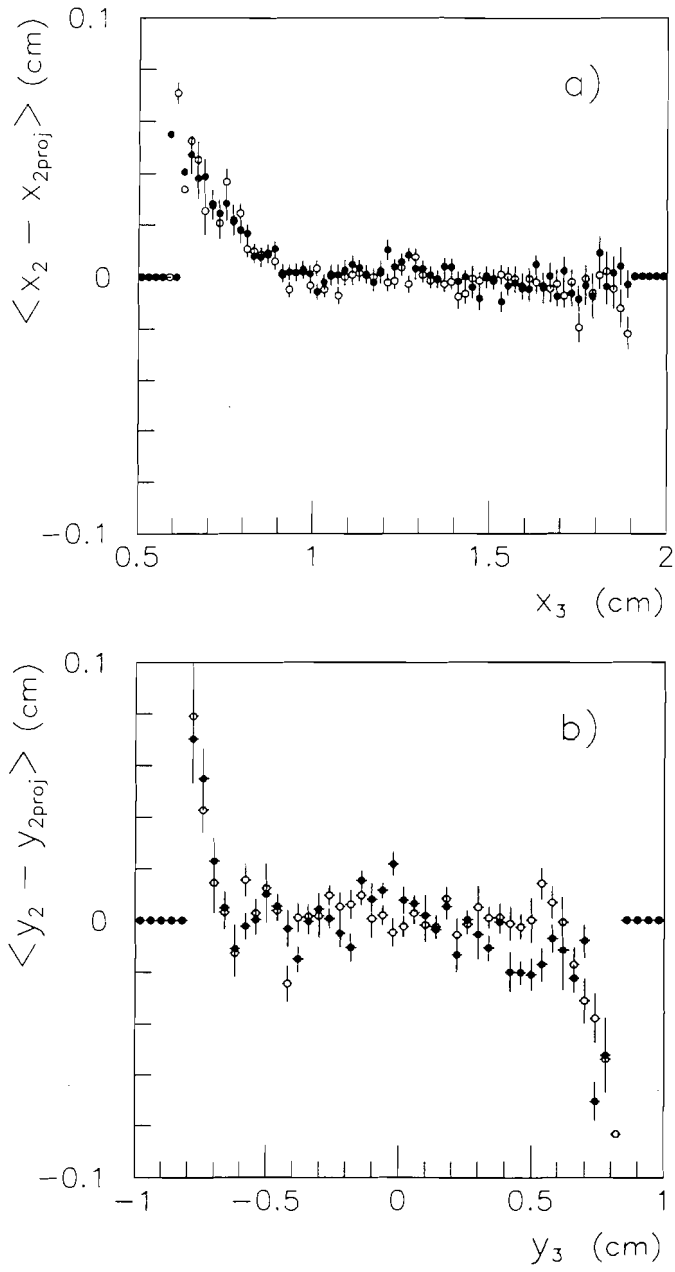

Figure 18: Mean value of the difference between the coordinate measured by S2 and the projected value, calculated using the coordinate measured by S3 and assuming the interaction point at (x,y,z)=(0,0,0), as a function of the coordinate measured by S3. (a) x-coordinate and (b) y-coordinate, for (•) data at $\sqrt{s}$=1800 GeV and (○) simulation.

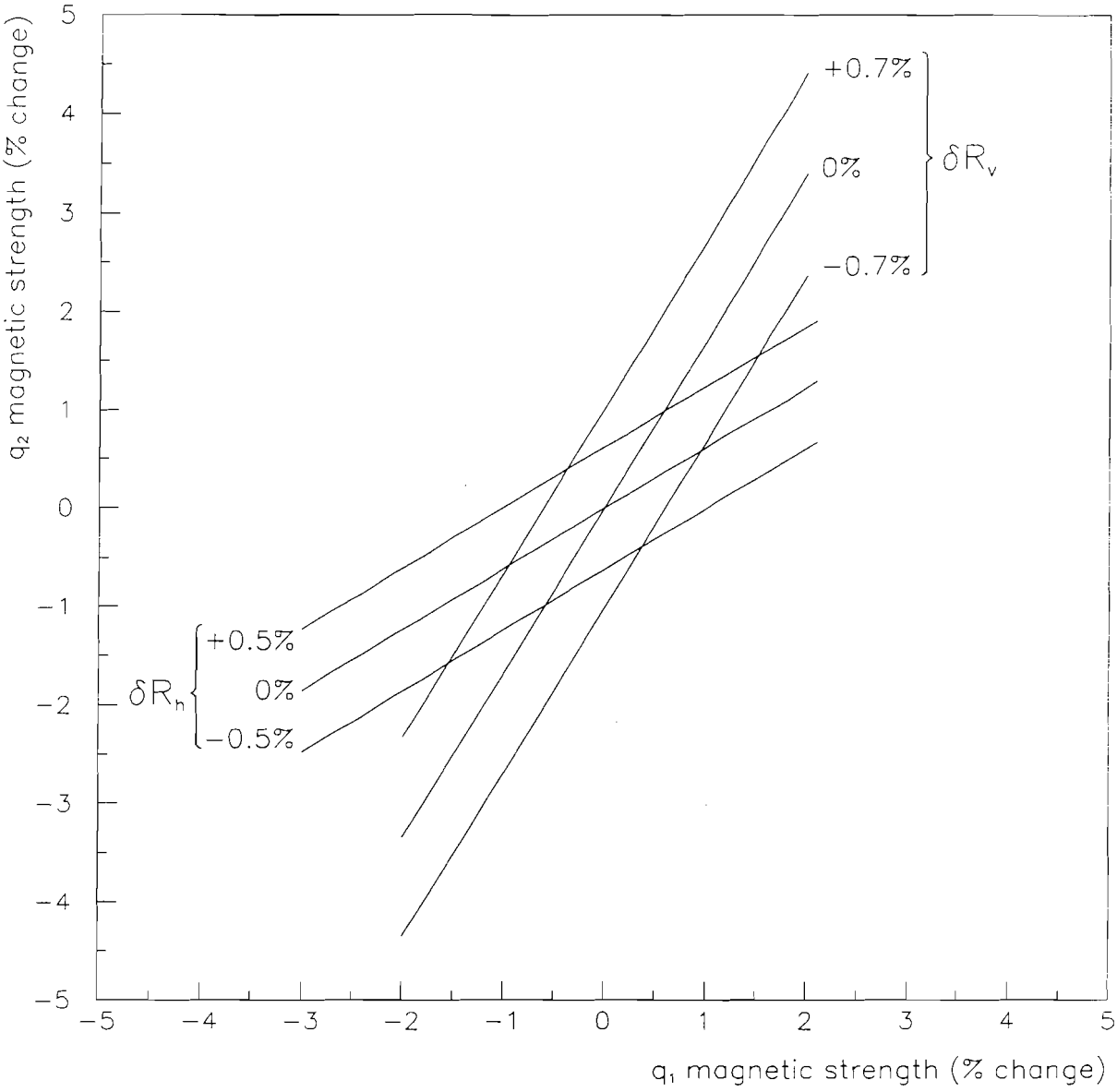

Figure 19: Isometric lines δR_h and δR_v in the (q_1,q_2) plane. The strengths of the quadrupole magnets q_1 and q_2 determine the vertical and horizontal focal lengths $L_{2(3)}^{v(h)}$ at S2 and S3; $\delta R_{v(h)}$ is the percentage change of the ratio of $R_{v(h)} = \frac{L_2^{v(h)}}{L_3^{v(h)}}$ as a function of the percentage change of the quadrupole magnetic strength. Lines are shown for the best determination of $R_{v(h)}$ and for the estimated errors. The intersection of the isometric lines corresponding to the δR_v and δR_h errors determines the uncertainty (1%) on the quadrupole magnetic strength at $\sqrt{s}$=1800 GeV.

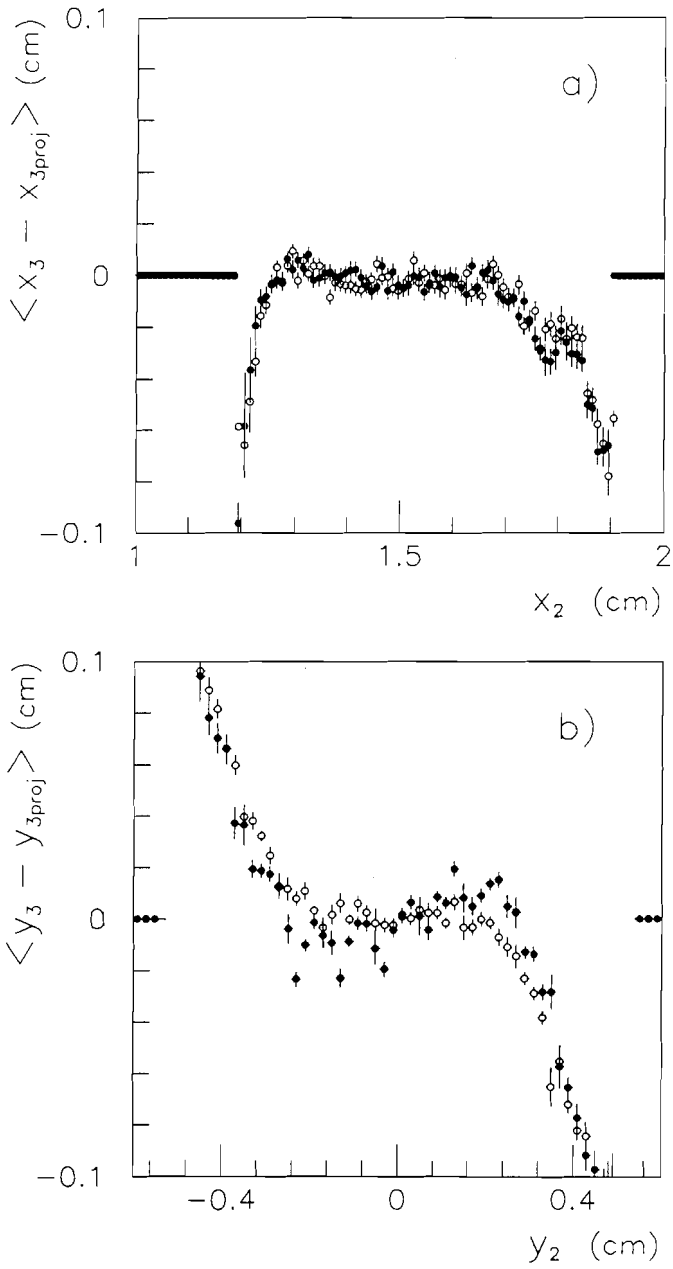

Figure 20: Mean value of the difference between the coordinate measured by S3 and the projected value, calculated using the coordinate measured by S2 and assuming the interaction point to be at (x,y,z)=(0,0,0), as a function of the coordinate measured by S2. (a) x-coordinate and (b) y-coordinate for (•) data at $\sqrt{s}$=546 GeV and (○) simulation.

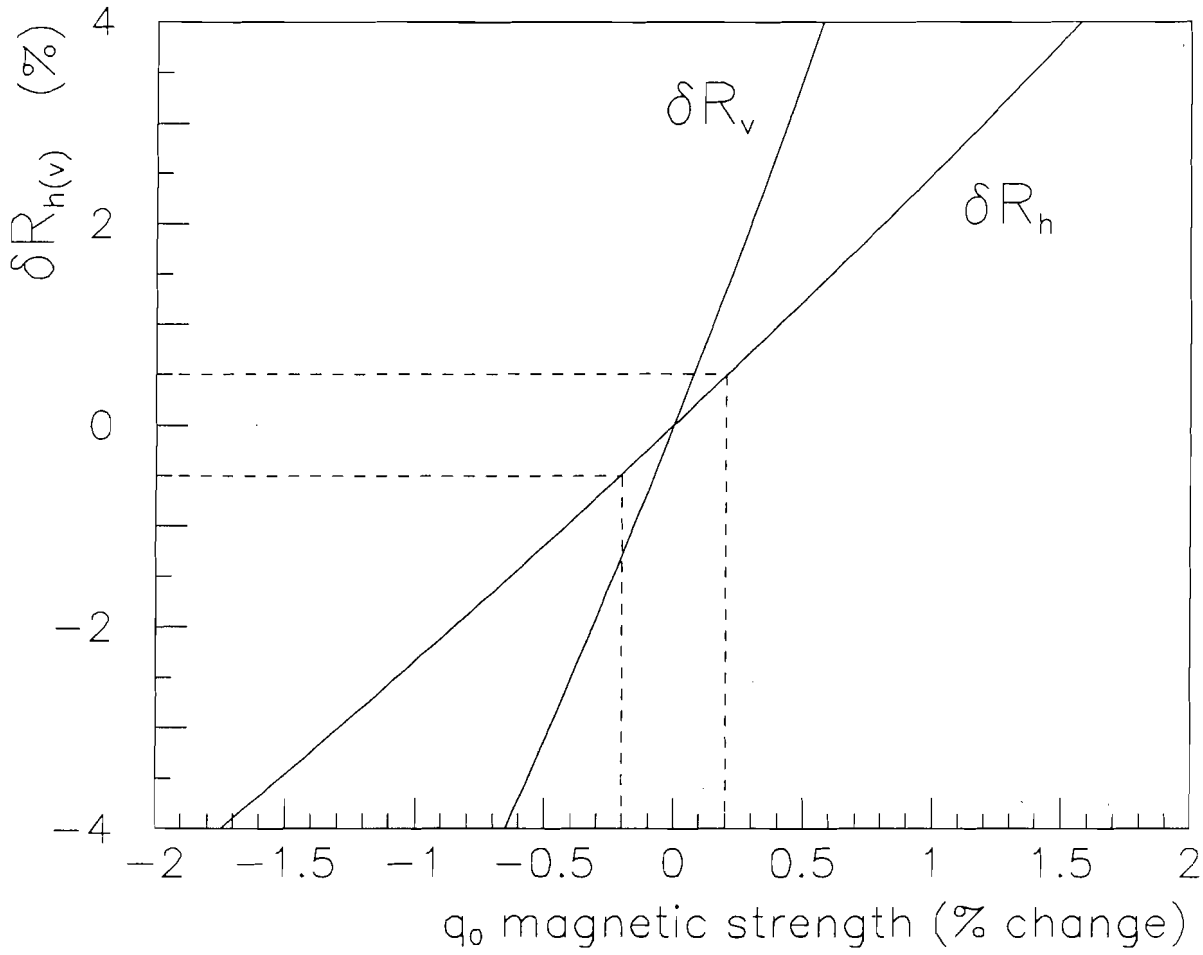

Figure 21: Dependence of δR_h and δR_v on the percentage change of the strength of the q_0 magnets at $\sqrt{s}$=546 GeV. $\delta R_{v(h)}$ is the percentage change of $R_{v(h)} = \frac{L_3^{v(h)}}{L_2^{v(h)}}$. The uncertainty on R_h (dashed lines) results in a 0.2% uncertainty on the low-β quadrupole magnetic strength.

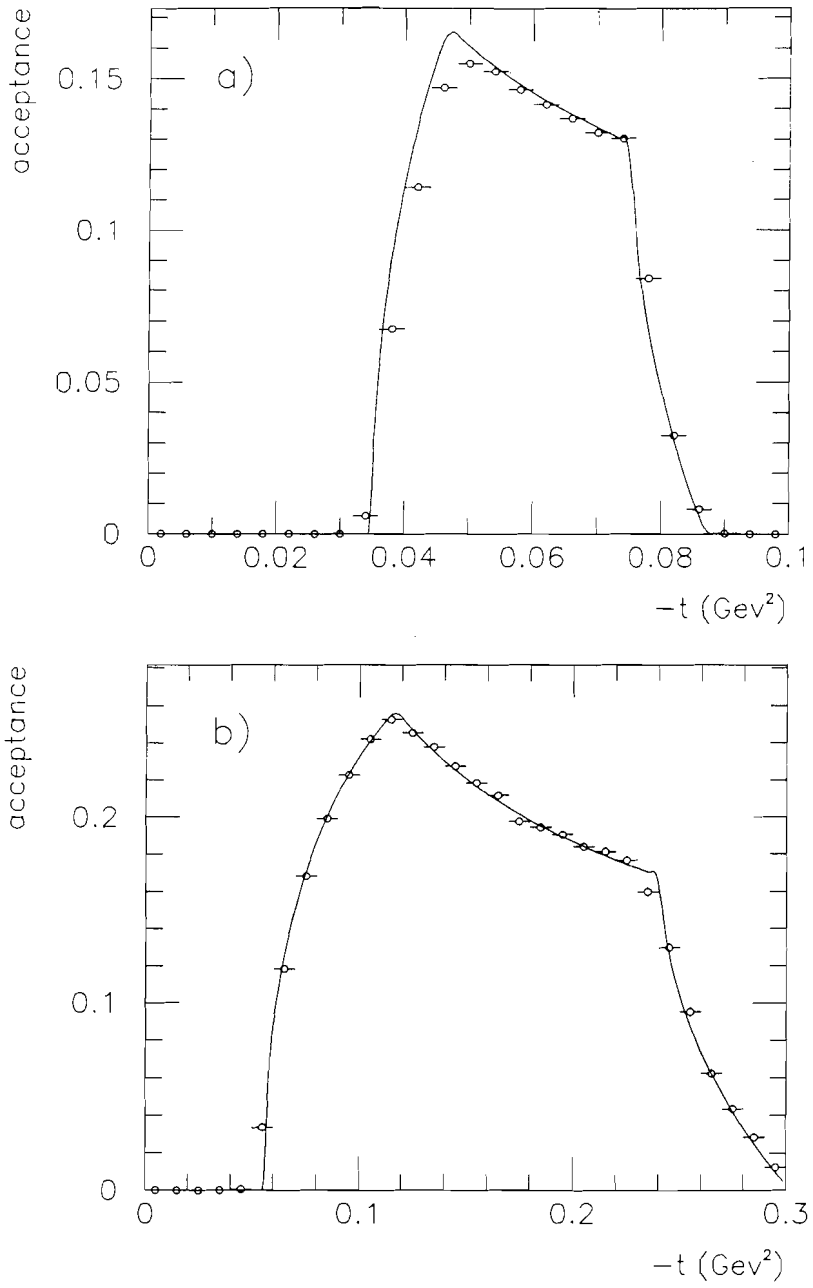

Figure 22: Spectrometer t-acceptance (o) calculated using the simulation, which accounts for all smearing effects at (a) $\sqrt{s}$=546 and (b) $\sqrt{s}$=1800 GeV. The solid line represents the t-acceptance calculated with eq.(2) of Appendix D.

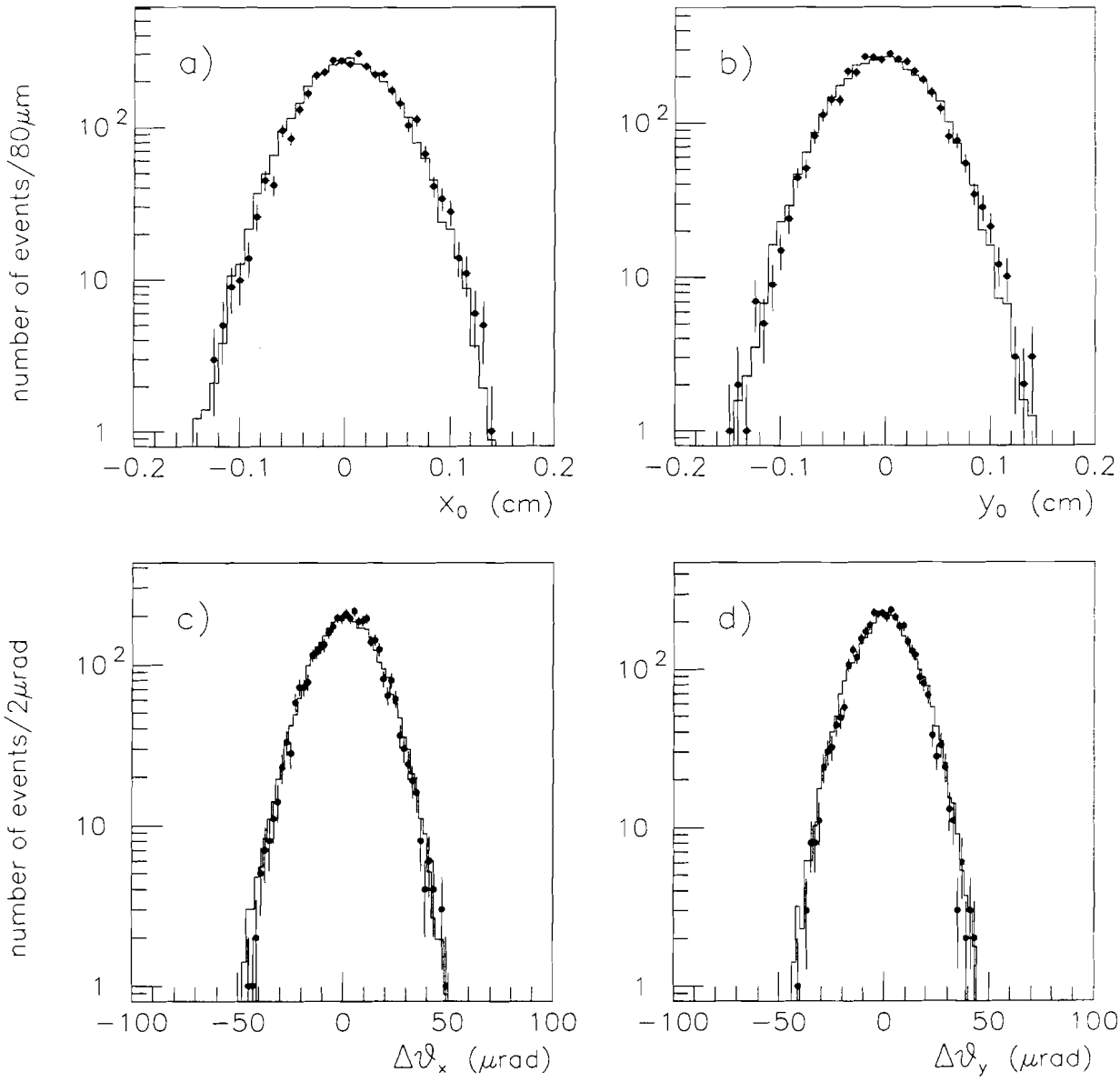

Figure 23: Comparison of distributions from data (•) and simulation (—) at $\sqrt{s}$=1800 GeV. (a,b) event origin (x_0,y_0); (c,d) collinearity ($\Delta\theta_x$, $\Delta\theta_y$), where $\Delta\theta = \theta^{\bar{p}} - \theta^{p}$.

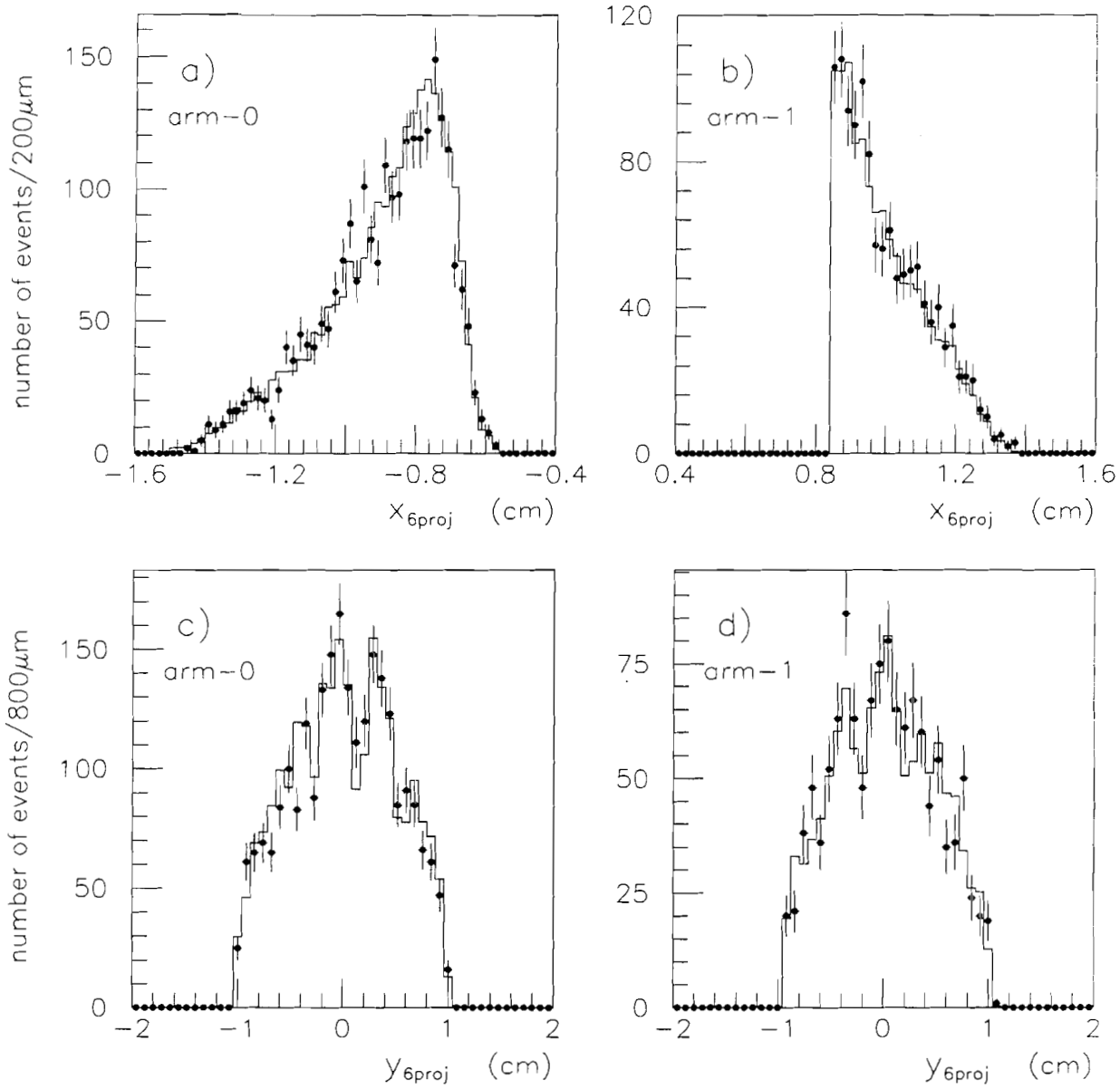

Figure 24: Comparison of distributions from data (•) and simulation (—) at $\sqrt{s}$=1800. (a,b): $x_{6proj}=L_6^h \cdot \theta_x^{\bar{p}}$; (c,d): $y_{6proj}=L_6^v \cdot \theta_y^{\bar{p}}$.